Single-cell spatial transcriptome reveals cell-type organization in the macaque cortex

Graphical abstract

Highlights

- A comprehensive cell-type taxonomy is constructed for the entire macaque cortex

- Stereo-seq reveals the global distribution of 264 cell types and their marker genes

- Regional density and composition of cell types are coupled with cortical hierarchy

- Cross-species analysis revealed primate-specific cell types enriched in layer 4
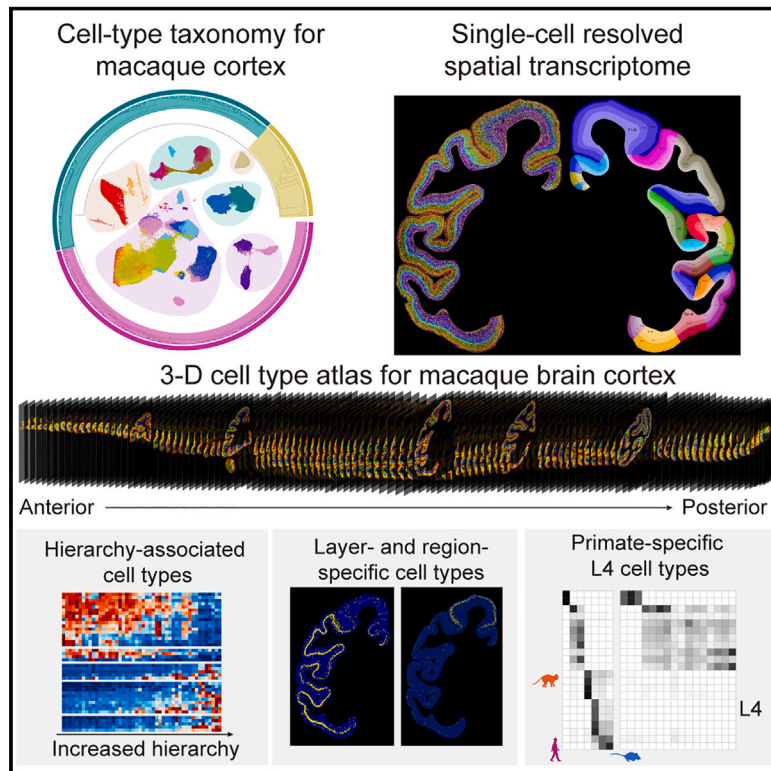
Authors

Ao Chen, Yidi Sun, Ying Lei, ...,
Zhiyong Liu, Xun Xu, Chengyu Li

Correspondence

ydsun@ion.ac.cn (Y.S.),
jianhuayao@tencent.com (J.Y.),
wuwei@lglab.ac.cn (W.W.),
liyuxiang@genomics.cn (Y.L.),
zmshen@ion.ac.cn (Z.S.),
liulongqi@genomics.cn (L.L.),
zhiyongliu@ion.ac.cn (Z.L.),
xuxun@genomics.cn (X.X.),
tonylicy@lglab.ac.cn (C.L.)

In brief

A spatially resolved single-cell transcriptome atlas of macaque cortex is generated that reveals the organization and evolution of primate cortical regions.

CellPress

Cell

Resource

Single-cell spatial transcriptome reveals cell-type organization in the macaque cortex

Ao Chen,[1,7,15,16,19] Yidi Sun,[2,19,*] Ying Lei,[1,10,19] Chao Li,[2,19] Sha Liao,[1,15,16,19] Juan Meng,[2,19] Yiqin Bai,[4,19] Zhen Liu,[5,19] Zhifeng Liang,[2,19] Zhiyong Zhu,[1,19] Nini Yuan,[2,19] Hao Yang,[2,19] Zihan Wu,[6,19] Feng Lin,[1] Kexin Wang,[2] Mei Li,[1] Shuzhen Zhang,[2] Meisong Yang,[1] Tianyi Fei,[2] Zhenkun Zhuang,[1,8] Yiming Huang,[2] Yong Zhang,[1,8] Yuanfang Xu,[2] Luman Cui,[1] Ruiyi Zhang,[2] Lei Han,[1] Xing Sun,[2] Bichao Chen,[1] Wenjiao Li,[1] Baoqian Huangfu,[1,8] Kailong Ma,[1] Jianyun Ma,[5] Zhao Li,[1] Yikun Lin,[2] He Wang,[2] Yanqing Zhong,[2] Huifang Zhang,[2] Qian Yu,[2] Yaqian Wang,[2] Xing Liu,[1] Jian Peng,[1] Chuanyu Liu,[1] Wei Chen,[1] Wentao Pan,[6] Yingjie An,[2] Shihui Xia,[2] Yanbing Lu,[2] Mingli Wang,[2] Xinxiang Song,[2] Shuai Liu,[1] Zhifeng Wang,[1] Chun Gong,[1,3] Xin Huang,[1] Yue Yuan,[1] Yun Zhao,[2] Qinwen Chai,[2] Xing Tan,[2] Jianfeng Liu,[2] Mingyuan Zheng,[2] Shengkang Li,[1,9] Yaling Huang,[1] Yan Hong,[1] Zirui Huang,[1] Min Li,[1] Mengmeng Jin,[2] Yan Li,[2] Hui Zhang,[2] Suhong Sun,[2] Li Gao,[5] Yinqi Bai,[1] Mengnan Cheng,[1] Guohai Hu,[3] Shiping Liu,[1,10] Bo Wang,[3] Bin Xiang,[5] Shuting Li,[2] Huanhuan Li,[2] Mengni Chen,[2] Shiwen Wang,[2] Minglong Li,[2] Weibin Liu,[1] Xin Liu,[1] Qian Zhao,[1] Michael Lisby,[7] Jing Wang,[1] Jiao Fang,[2] Yun Lin,[1] Qing Xie,[1] Zhen Liu,[2,13] Jie He,[2] Huatai Xu,[4] Wei Huang,[2] Jan Mulder,[11,18] Huanming Yang,[1] Yangang Sun,[2] Mathias Uhlen,[11,18] Muming Poo,[2,13] Jian Wang,[1,3] Jianhua Yao,[6,*] Wu Wei,[4,5,*] Yuxiang Li,[1,17,*] Zhiming Shen,[2,13,*] Longqi Liu,[1,10,*] Zhiyong Liu,[2,13,*] Xun Xu,[1,12,*] and Chengyu Li[2,13,14,20,21,*]

[1]BGI-Shenzhen, Shenzhen 518103, China
[2]Institute of Neuroscience, State Key Laboratory of Neuroscience, CAS Center for Excellence in Brain Science and Intelligence Technology, University of Chinese Academy of Sciences, Chinese Academy of Sciences, Shanghai 200031, China
[3]China National GeneBank, BGI-Shenzhen, Shenzhen 518120, China
[4]Lingang Laboratory, Shanghai 200031, China
[5]CAS Key Laboratory of Computational Biology, Shanghai Institute of Nutrition and Health, University of Chinese Academy of Sciences, Chinese Academy of Sciences, Shanghai 200031, China
[6]Tencent AI Lab, Shenzhen 518057, China
[7]Department of Biology, University of Copenhagen, Copenhagen 2200, Denmark
[8]School of Biology and Biological Engineering, South China University of Technology, Guangzhou 510006, China
[9]Guangdong Bigdata Engineering Technology Research Center for Life Sciences, Shenzhen 518083, China
[10]BGI-Hangzhou, Hangzhou 310012, China
[11]Department of Protein Science, Science for Life Laboratory, KTH-Royal Institute of Technology, Stockholm 17121, Sweden
[12]Guangdong Provincial Key Laboratory of Genome Read and Write, Shenzhen 518120, China
[13]Shanghai Center for Brain Science and Brain-Inspired Technology, Shanghai 201602, China
[14]School of Future Technology, University of Chinese Academy of Sciences, Beijing 100049, China
[15]BGI Research-Southwest, BGI, Chongqing 401329, China
[16]JFL-BGI STOmics Center, Jinfeng Laboratory, Chongqing 401329, China
[17]BGI Research-Wuhan, BGI, Wuhan 430074, China
[18]Department of Neuroscience, Karolinska Institute, Stockholm 17177, Sweden
[19]These authors contributed equally
[20]Present address: Lingang Laboratory, Shanghai, China
[21]Lead contact
*Correspondence: ydsun@ion.ac.cn (Y.S.), jianhuayao@tencent.com (J.Y.), wuwei@lglab.ac.cn (W.W.), liyuxiang@genomics.cn (Y.L.), zmshen@ion.ac.cn (Z.S.), liulongqi@genomics.cn (L.L.), zhiyongliu@ion.ac.cn (Z.L.), xuxun@genomics.cn (X.X.), tonylicy@lglab.ac.cn (C.L.)
https://doi.org/10.1016/j.cell.2023.06.009

SUMMARY

Elucidating the cellular organization of the cerebral cortex is critical for understanding brain structure and function. Using large-scale single-nucleus RNA sequencing and spatial transcriptomic analysis of 143 macaque cortical regions, we obtained a comprehensive atlas of 264 transcriptome-defined cortical cell types and mapped their spatial distribution across the entire cortex. We characterized the cortical layer and region preferences of glutamatergic, GABAergic, and non-neuronal cell types, as well as regional differences in cell-type composition and neighborhood complexity. Notably, we discovered a relationship between the regional distribution of various cell types and the region's hierarchical level in the visual and somatosensory systems. Cross-species comparison of transcriptomic data from human, macaque, and mouse cortices further revealed primate-specific cell types that are enriched in layer 4, with their marker genes expressed in a region-dependent manner. Our data provide a cellular and molecular basis for understanding the evolution, development, aging, and pathogenesis of the primate brain.

INTRODUCTION

The brain comprises diverse cell types that are interconnected to form specific neural circuits underlying cognition and behavior. Primates tend to have a larger cortex relative to their body size, in line with their higher cognitive and social abilities.[1] The macaque brain comprises over six billion cells, which could be classified into hundreds of cell types based on their spatial, molecular, morphological, or physiological features.[2–6] These diverse cell types are located in hundreds of distinct brain regions defined by anatomical, histological, and functional characteristics.[7] Understanding the composition and spatial distribution of various cell types in the cortex is essential for elucidating the organization principles of the primate brain.

Advances in single-cell transcriptome analyses have uncovered the gene expression profiles of diverse cell types in the brain of various species.[3,8–14] Comparative studies also revealed adaptations in neuronal types throughout evolution.[8,11,12,15–18] Recently developed spatial transcriptomic technologies have provided new tools for mapping the spatial distribution of gene expression in the brain.[19–27] Spatial transcriptome analysis of the whole primate brain at the single-cell resolution is highly challenging because of the heterogeneity and large brain size, as well as the difficulty of preserving cellular organization in large and thin tissue sections.

In this study, we employed a newly developed large-field-of-view spatial transcriptome method, termed "stereo-seq,[28]" and developed a method for preparing centimeter-scale thin sections of the monkey brain. In combination with a large-scale single-nucleus RNA sequencing (snRNA-seq) analysis, we obtained a comprehensive 3D single-cell atlas for the cortex of cynomolgus monkey. This enabled a systematic analysis of the cortical-layer- and region-specific distributions of cell types and their molecular fingerprints and discovery of the relationship between cell-type composition and hierarchical organization of the visual and somatosensory systems. Cross-species comparison also uncovered primate-specific cell types. The dataset is open for access via https://macaque.digital-brain.cn/spatial-omics.

RESULTS

Transcriptomic taxonomy of cell types in the macaque cortex

We first characterized single-cell taxonomy across the cortex of three adult male cynomolgus monkeys, using a droplet-based snRNA-seq method.[29,30] A total of 1,493,240 cells from 143 regions of the entire cerebral cortex of two monkeys were used for snRNA-seq analysis and cell-type classification. The molecular fingerprints of classified cell types were then used for cell-type identification in the stereo-seq maps described below. For the anatomical parcellation of brain regions, we also performed immunostaining on sections adjacent to stereo-seq sections (Figures 1A and S1A–S1F).

For snRNA-seq analysis, we used cortical tissues from two cynomolgus monkey brains. In monkey #1, 646,393 cells were obtained from 50-μm coronal sections adjacent to those used for stereo-seq. In monkey #2, 846,847 cells were obtained

from dissected block-face cortical regions of the hemisphere contralateral to that used for stereo-seq. Transcriptome profiles of single cells from the two monkeys were integrated and subjected to dimensionality reduction and clustering analysis. This led to the identification of 264 cell clusters for 143 cortical regions, which were grouped into 9 conventional lobes (prefrontal, frontal, occipital, temporal, parietal, auditory, somatosensory, cingulate, and insular; Figure 1B; Table S1). Most cell clusters included cells from both monkeys and multiple cortical regions, indicating the reproducibility of our clustering results (Figure S1G). The reliability of clustering was also validated by Jaccard similarity analysis (Figure S1H) and random forest analysis (Figure S1I).

We further constructed a three-level taxonomy tree using the hierarchical clustering of these cell types (Figure 1B; Table S2). Level 1 represents three major cell classes: glutamatergic (969,794), GABAergic (268,097) and non-neuronal (97,298) cells. Level 2 comprised subclasses of these three major classes, each with distinct subclass marker genes (Figures 1B, S1J, and S1K). Based on their gene expression profiles and localization in the stereo-seq map (see section below), glutamatergic neuron subclasses were annotated by their layer preferences (L for layer: L2, L2/3, L2/3/4, L3/4, L3/4/5, L4, L4/5, L4/5/6, L5/6, and L6; see STAR Methods). The glutamatergic neuron subclasses showed substantial correspondence with the projection-property-inferred subclasses identified by the Allen Institute[16] (Figure S1L). GABAergic neuron subclasses were annotated by 5 prominent marker genes: lysosome-associated membrane protein 5 (*LAMP5*), vasoactive intestinal peptide (*VIP*), reelin (*RELN*), parvalbumin (*PV*), and somatostatin (*SST*).[12,15,16] We noted that the interneuron marker gene calbindin (*CALB1*) is mainly expressed by SST and LAMP5 subclasses, and the calretinin gene (*CALB2*) is mainly expressed by VIP and VIP_RELN subclasses (Figure S1K). The 6 non-neuronal subclasses included astrocytes (ASCs), oligodendrocyte precursor cells (OPCs), oligodendrocytes (OLGs), microglia (MG), endothelial cells (ECs), and vascular leptomeningeal cells (VLMCs), each annotated by their specific marker genes (Figure S1K). Level 3 represents further classification of subclasses, including 264 cell clusters (termed hereafter "types"). Each level 3 cell type was annotated by level 1 and 2 labels and two top-rank differentially expressed genes (DEGs, Table S2). For example, the third type of glutamatergic cells found in L2 that highly expressed *ART3/GPC5* was annotated as Glu L2.3-*ART3/GPC5*. For the sake of brevity, the cell-type name was simply referred to without marker genes in the figures, e.g., Glu L2.3-*ART3/GPC5* as L2.3. This snRNA-seq analysis incorporating spatial transcriptome information yielded a comprehensive cell-type taxonomy of the macaque cerebral cortex.

Spatial distribution of diverse cell types across the macaque cortex

We used stereo-seq to capture mRNAs from all cells of each brain section in close contact with a large silicon chip (up to 5 cm × 3 cm), which comprised regular 2D arrays of DNA nanoballs (DNBs; size, 220 nm; center to center, 500 nm). We developed a section-flattening method after cryo-sectioning to obtain even and smooth surface contact between large brain sections

A

B
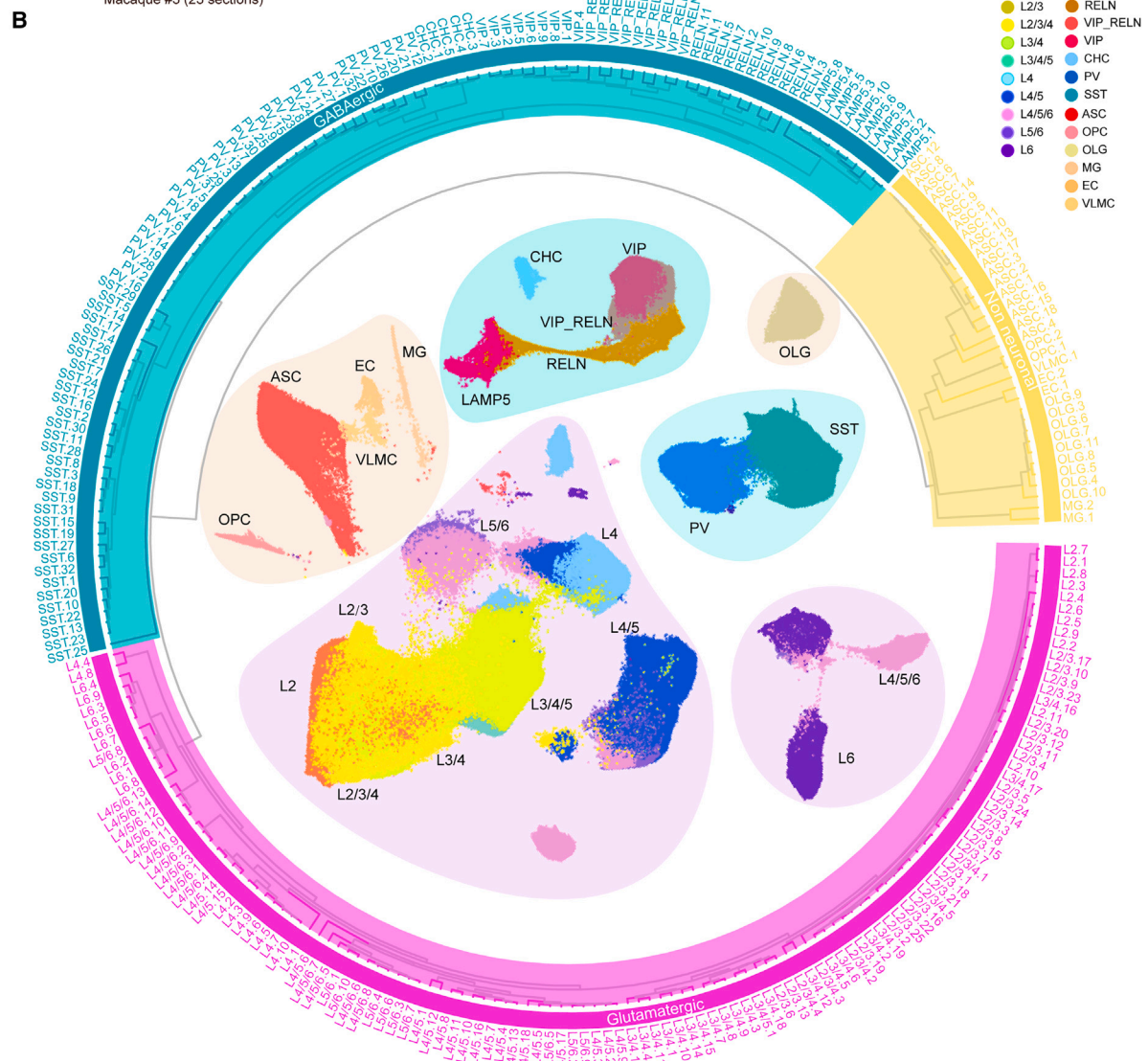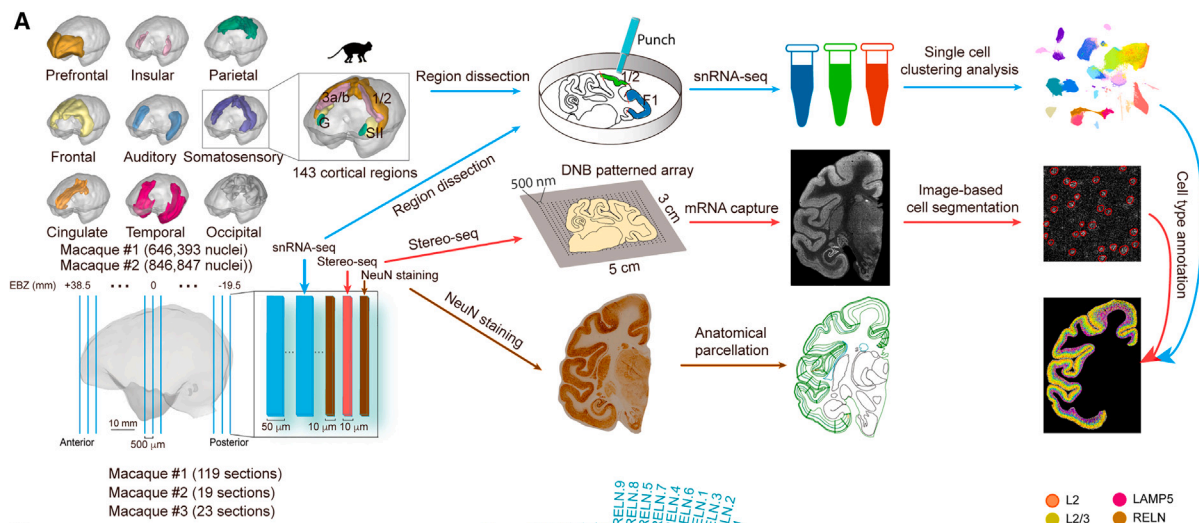
(legend on next page)

and stereo-seq chips (see STAR Methods). Stereo-seq analysis was performed on 10-μm coronal sections from the freshly isolated left hemisphere of three adult male cynomolgus monkeys. In monkey #1, we obtained a total of 119 sections at 500-μm spacing covering the entire cortex (Table S3), together with two 10-μm sections adjacent to each stereo-seq section for immunostaining and several adjacent 50-μm thick sections for regional microdissection and snRNA-seq analysis (see above, Figure 1A). For biological replication, we also obtained 10-μm sections from two other monkeys (19 sections from #2 and 23 sections from #3, 3-mm spacing; Table S3). The 10-μm section thickness, together with section preservation procedures that reduced mRNA diffusion, facilitated spatial transcriptome analysis at the single-cell resolution.

Each stereo-seq section was stained with a dye specific to nucleic acid[28] and a fluorescence-labeled lectin, concanavalin A (ConA), that marks the plasma membrane (Figures 2A and S2A). An artificial intelligence (AI)-assisted automatic segmentation method was developed for single-cell identification based on nucleic acid and ConA images (see STAR Methods and Table S4). The reliability of automatic identification was shown by high recall and precision rates (Figures 2B and S2B). Using this method, we obtained 266,310 segmented cortical cells per section with an average of 819 unique molecular identifiers (UMIs) and 458 genes per cell (Figure 2C; Table S3). The average number of genes per cell was much higher than that in background (1.5 ± 0.9 genes/bin) and that in 10 μm × 10 μm bins (each containing 20 × 20 DNBs; 147 ± 82 genes/bin) across entire sections (Figure 2C).

To register and annotate spatially resolved single cells in stereo-seq spatial transcriptome maps, we applied a recently developed supervision-based cell typing method[31] (Figure S2C; see STAR Methods). Using this method, we identified cell types for 42,076,954 cortical cells in the spatial transcriptome map. The robustness of cell annotation is evidenced by high correlation value between the gene expression profiles of annotated cell types and those of snRNA-seq-defined cell types (Figure S2D). Molecularly defined, single-cell resolved 3D cell-type maps of the cortex were then constructed for all three monkeys, and high consistency of these maps was observed between adjacent sections and biological replicates (Figures 2D and S2E–S2H). Images of five representative cortical sections along anterior-posterior (A-P) axis are shown in Figure 2D (lower), revealing the distribution of 23 cell subclasses. As expected, we found that many cell subclasses showed clear laminar preferences, as illustrated by a zoomed-in image and the density profiles of all cell subclasses along the axis perpendicular to the cortical sheet of secondary somatosensory area (SII; Figure 2E). The laminar distribution of various cell subclasses agrees with the layer-specific profile of the corresponding marker genes, *C1QL2* for L2, *ADCYAP1* for L2/3, *IL1RAPL2* for L4, *HTR2C* for L4/5/6, and *RXFP1* for L5/6 (Figures 2F, S2I, and S2J).

The brain-wide stereo-seq map of diverse cell types allowed us to further examine cell-type compositions in each cortical region. Unsupervised clustering analysis revealed that 9 major cortical lobes could be distinguished by their cell-type compositions based on the stereo-seq map (Figure 2G) and snRNA-seq data (Figure S2K). Cells close to each other tend to have higher probabilities of forming synaptic connections.[32,33] We noted that different cell types were locally intermixed on the spatial transcriptome map (Figure 2H), suggesting that differential local circuits could originate from distinct local cell composition. Therefore, we quantified the "neighborhood complexity" of local cell-type composition in various cortical layers (see STAR Methods) and found that the complexity in deeper cortical layers was higher than that in upper layers (Figures 2I and S2L). Notably, for the neighborhood complexity of each layer, we found distinct differences among cortical regions, as illustrated for a representative region from each of the 9 cortical lobes (Figures 2J and S2L). Therefore, cell types exhibited neighborhood-composition specificity in different layers and regions.

## Cell-type composition and distribution correlate with cortical hierarchy

Further analysis of our stereo-seq cell-type maps showed marked cell density differences among various cortical regions, with the highest density in V1 (~1,500 cells/μm²) and the lowest density in the entorhinal cortex (Elc; ~200 cells/μm²) (Figure S3A). In line with the notion that higher-level regions in the anatomical hierarchy exhibit lower cell densities, we found a significantly negative correlation between cell densities and hierarchical levels that were previously defined for the primate visual and somatosensory systems[34] (Figures 3A, 3B, S3B, and S3C). Unsupervised clustering analysis revealed that regions of the same hierarchical level exhibited similar cell-type composition profiles in both sensory systems (Figures 3C, 3D, and S3D).

To uncover cell types important for the observed hierarchy-dependent variation in cell-type compositions, we calculated Pearson's correlation coefficients between the percentages of each cell type and hierarchical levels of various cortical regions (see STAR Methods). This allowed us to identify sets of glutamatergic, GABAergic, and non-neuronal cell types that exhibited negative or positive correlation with hierarchical levels (Figures 3E, 3F, and S3E). The distribution of these cell types could be visualized in the reconstructed 3D maps for monkey #1 (Figure 3G). Interestingly, many negatively correlated glutamatergic cell types were common in both systems; i.e., they were preferentially localized to the early sensory pathways (labeled red in Figures 3E and 3F). Marker genes of these cell types were enriched in the gene ontology (GO) terms of calcium ion binding, trans-synaptic signaling, and ion channel activity (Figures S3F and S3G). In contrast, only a single GABAergic cell type showed negative correlation with the hierarchical level in both systems (SST.18 *ADAMTS6/ESM1*). Furthermore, four

---

Figure 1. Transcriptomic cell-type taxonomy of the macaque cortex

(A) Overall experimental design. For snRNA-seq, single nuclei from 143 cortical regions were isolated by micro-dissections of tissue sections from macaque monkey #2 (left top), together with sections adjacent to stereo-seq sections in monkey #1 (left below).

(B) Uniform manifold approximation and projection (UMAP) of snRNA-seq clustering and cell-type taxonomy of the macaque cortex.

See also Figure S1 and Tables S1 and S2.
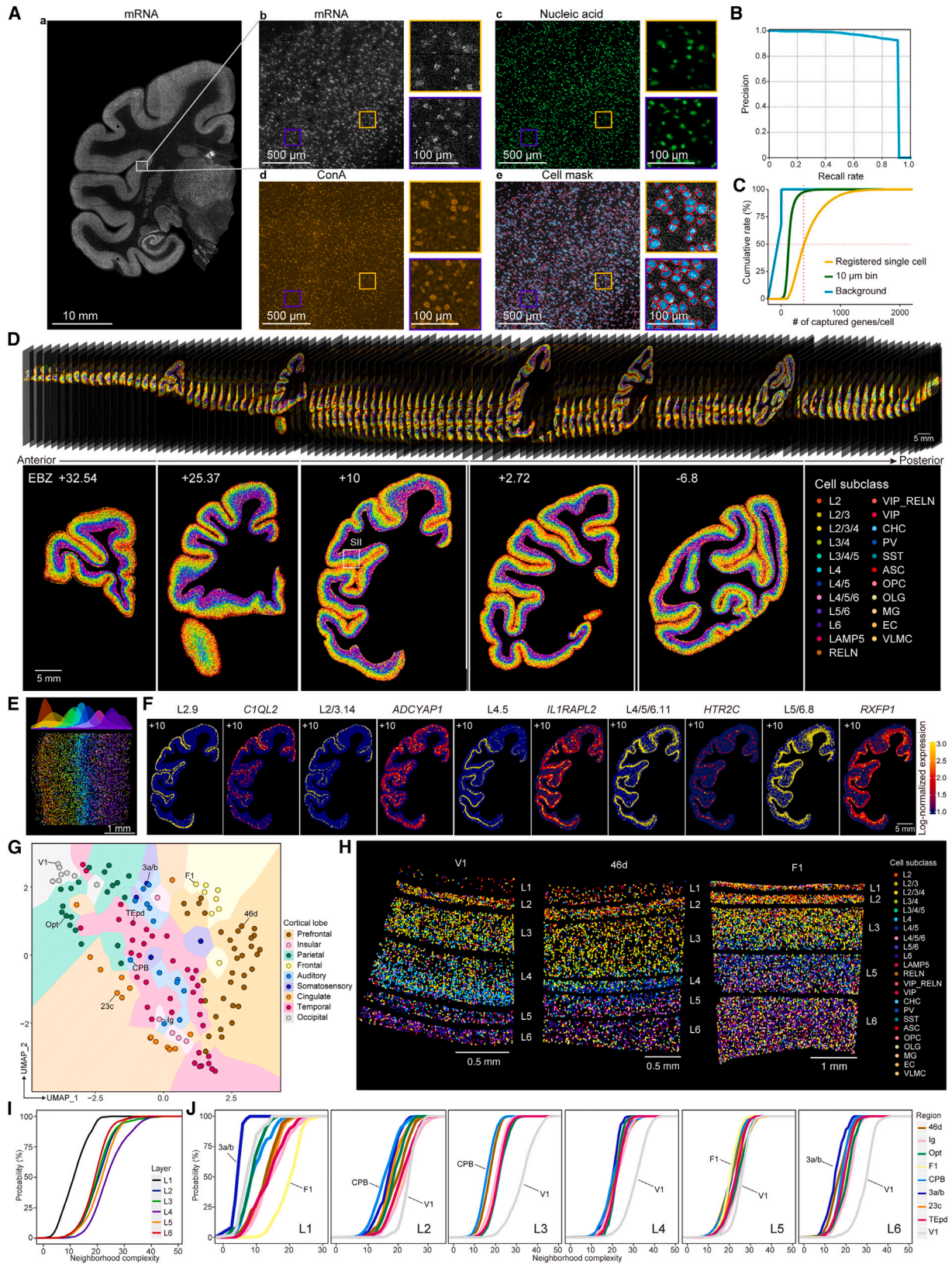
glutamatergic, five GABAergic, and one non-neuronal cell types showed distributions that positively correlated with the hierarchical level in both systems (Figure S3E). Genes highly expressed in the latter glutamatergic cell types were associated with the GO terms of neuron projection and dendritic spine (Figure S3G). The consistency of hierarchy-associated cell types in the two sensory systems implicates a general rule for cellular organization in the macaque brain.

Spatial organization of glutamatergic neurons

Glutamatergic neurons account for the largest population of neurons in the macaque cortex (Figure 1B) and exhibited clear laminar preference across regions (Figures 2D–2F and 4A), consistent with previous findings in mice and primates.[8,35–37] We calculated the relative percentage of a specific cell type among 9 cortical lobes and Shannon entropy value (the extent of cell dispersal) for each cell type. Both parameters indicated that several cell types were predominantly in specific lobes (Figure 4A).

Based on distribution profiles calculated from relative cell density, we found that all glutamatergic cell types showed some degree of preferential distribution along A-P gradient (Figure 4B). We further zoomed in to the regional distribution of each glutamatergic cell type (Table S5) and found that nine glutamatergic cell types were highly localized to specific cortical regions (Figures 4C, 4D, and S4A). Four glutamatergic cell types (L4.4 *KCNH8/PDE3A*, L3/4.7 *HPSE2/TENM2*, L4.8 *NTNG1/PHACTR2*, and L6.7 *SEMA3E/HS3ST4*) were predominantly localized to V1, two (L2/3.7 *COL5A2/TESPA1* and L3/4.10 *PHLDB2/SNTG2*) to F1, and three (L2.1 *CCBE1/EPHA6*, L2/3.9 *FAM19A1/LRRTM4*, and L4.3 *ILRAPL2/TSHZ2*) to the temporal pole. Since the marker genes of these cells were identified by snRNA-seq, their region-specific expression in the stereo-seq map further validated the reliability of cell-type identification in this study (Figures 4E, 4F, and S4B). For example, V1-specific cell types were characterized by a high expression of *NTNG1*, which is known to guide axon growth during neuronal development, and its polymorphism was associated with schizophrenia.[38] The region-specific expression of *NTNG1* was also validated by RNAscope (Figure 4G). Using neighborhood composition analysis as described above (Figure 4H), we found that these region-specific glutamatergic cell types also showed distinct clusters of neighborhood compositions and layer specificity for V1, F1, and temporal pole regions (Figure 4I). Taken together, our results uncovered layer and region specificities in the distribution and composition of glutamatergic cell types in the macaque cortex.

Given that glutamatergic receptors are essential for driving information processing in cortical circuits and serve as potent drug targets in many brain diseases,[39] we further mapped the spatial distribution of these genes and found that the subunits of AMPA, Kainate, Delta, NMDA, and metabotropic glutamate receptors showed differential expression patterns among various cortical layers and regions (Figures 4J, S4C, and S4D). Notably, we found that many glutamatergic receptor genes exhibited expression levels positively correlated with the hierarchical levels of various cortical regions in both sensory systems (Figures 4J and S4D). For example, *GRIN2B* expression increased with hierarchical level in both visual and somatosensory systems, in line with a computational analysis showing increasing NMDAR-GluN2B expression along the cortical hierarchy in humans.[40] In addition, the association between subunit expression and hierarchy was layer specific; for example, *GRIA4* showed positive correlation only in L2/3, whereas *GRM3* showed that correlation in L4–L6 (Figures 4J and S4D).

Spatial organization of GABAergic neurons

We next examined the layer and regional specificities of GABAergic cells and found that RELN subclass was predominantly located in L1/2, whereas LAMP5, VIP, and VIP_RELN subclasses were enriched in L2/3/4. PV and SST subclasses were dispersed across L2 to L6, and chandelier subclass (CHC) was enriched in L2 and L4 (Figure 5A). All GABAergic neuron types were distributed across nine cortical lobes with various degrees of specificity: the fraction of each GABAergic subclass was lower in visual cortices (V1–V4); PV subclass was higher in motor cortices (F1–F7) and the entorhinal area; and CHC, RELN, and VIP subclasses were prominent in the prefrontal and cingulate cortices (Figures 5B and S5A–S5C; Table S5). A similar distribution of CHC cells was found in the human cortex.[41]

The fine stereo-seq maps allowed us to uncover spatial heterogeneity within GABAergic subclasses. As an example, SST cells were selectively distributed in L2/3, L3, L3/4/5, L5, and L5/6 and exhibited distinct gene expression and GO terms

---

Figure 2. Single-cell spatial transcriptome map of the macaque cortex

(A) Single-cell segmentation for stereo-seq analysis. (Aa) Total mRNA captured from an example section (ear bar zero [EBZ] coordinate +12.01 mm). (Ab) Left: total mRNA of the enlarged area in (Aa). Right: enlarged orange and purple boxes showing mRNA aggregates. (Ac and Ad) Staining for nucleic acid (Ac) and ConA (Ad) for the areas as in (Ab). (Ae) AI-assisted automatic segmentation based on nucleic acid and ConA staining. Red circles, boundaries of segmented cells; blue dots, mRNAs inside cells.

(B) Recall and precision rates of cell segmentation for the region shown in (Ab).

(C) Cumulative percentage of the distribution of genes captured per cell for all registered single cells, for regions outside the segmented cells ("background"), and for 10 μm × 10 μm binned areas ("10-μm bin").

(D) Spatial distribution of 264 cell types organized in 23 cell subclasses in all coronal sections (top) and five example sections (bottom) from monkey #1 along the A-P axis.

(E) Spatial map (bottom) and density profiles (top) of cell subclasses from SII (white box in D), color coded as in (D).

(F) Spatial map of five example cell types and marker genes for an example section (EBZ +10 mm) of monkey #1.

(G) UMAP plot of regional cell-type compositions.

(H) Spatial maps of cell subclasses in V1, 46d, and F1.

(I and J) Neighborhood complexity of cell types in various cortical layers for all regions (I) and nine example regions (J).

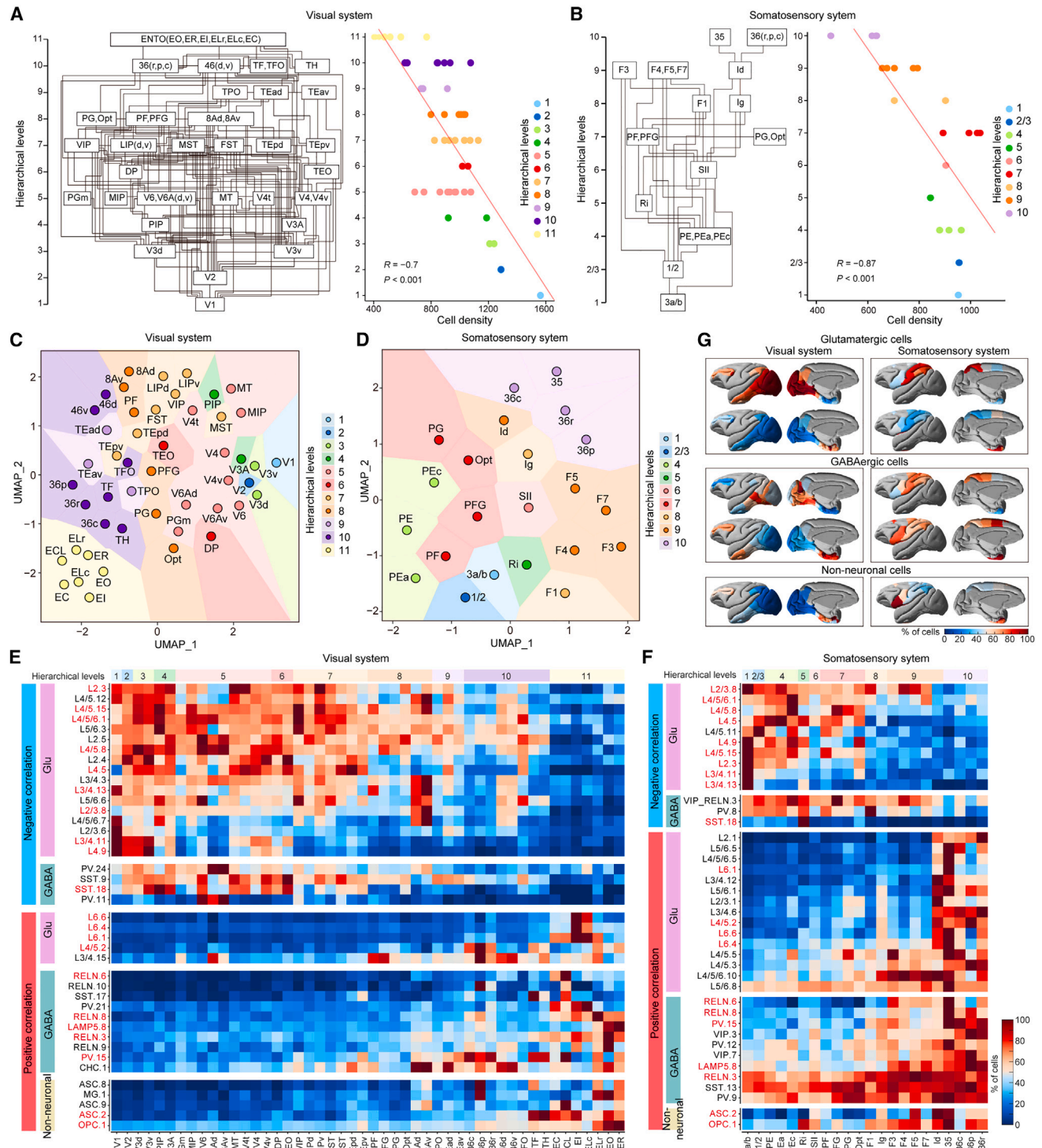See also Figure S2 and Tables S3 and S4.

**Figure 3. Association between cell-type distribution and cortical hierarchy**

(A and B) Hierarchical levels of visual (A) and somatosensory (B) systems, as defined by Felleman and Van Essen.[34] Right: cell densities in the indicated brain regions ordered by hierarchical levels.

(C and D) Cell density UMAP, showing the region clusters of different hierarchical levels.

(E and F) Heatmaps showing the regional density of individual cell types exhibiting positive or negative correlation with the hierarchical level.

(G) 3D surface rendering of the percentages of each major class shown in (E) and (F).

See also Figure S3.
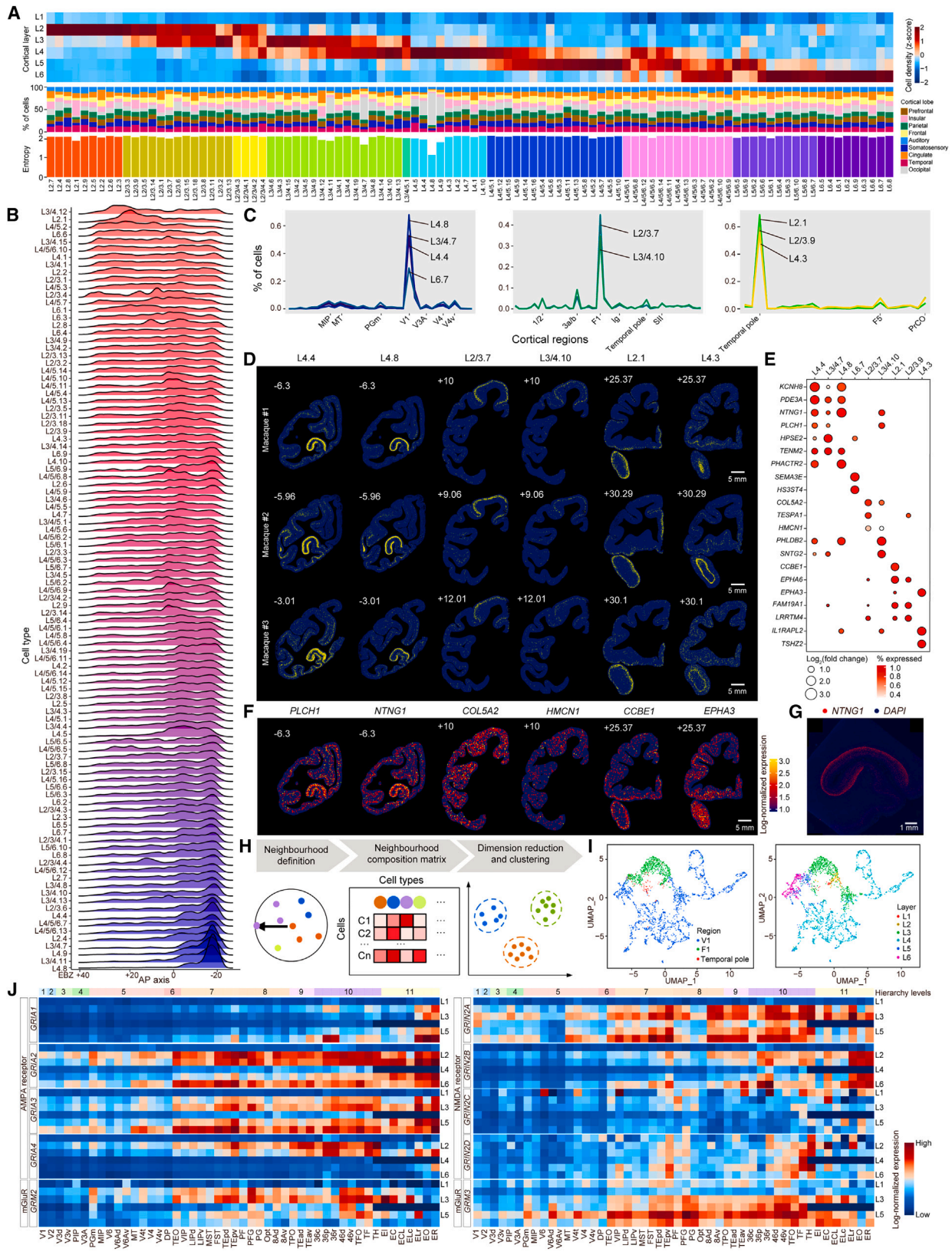
(legend on next page)

(Figures S5D–S5G). We found two groups of SST cell types that showed "complementary abundance" in the macaque cortex: group 1 exhibited high density in the prefrontal and cingulate cortices, whereas group 2 mainly populated in the occipital and parietal cortices (Figure 5C). Group 1 showed higher density in L2 and L5, whereas group 2 peaked only in L2 (Figure S5H). The two SST groups were also distinguished by gene expression patterns and GO terms (Figures 5D and S5I). All 143 cortical regions could be clustered into 9 cortical lobes based on the relative density of these SST cell groups (Figure 5E).

Chandelier cells innervate the axon initial segments (AISs) of pyramid neurons and could veto neuronal firing.[42] Among the three chandelier cell types, CHC.3 was the most abundant in L2, whereas CHC.1 and CHC.2 were dispersed among all layers and the most abundant in L4 (Figure 5F). Cell adhesion molecules were specifically upregulated in CHC.3 (CDH6, CDH20, and PCDH17), whereas kainite (GRIK1) and nicotinic (CHRNA5) receptor genes were highly expressed in CHC.1 and CHC.2 cells (Figure 5G). Neighborhood analysis showed that 30 out of 122 glutamatergic cell types were co-localized with all three CHC types (Figure S5J; Table S6). Furthermore, the neighborhood composition of glutamatergic cell types was similar between CHC.1 and CHC.2 cell types and distinct from that of CHC.3 cells (Figure 5H). In most cortical regions, glutamatergic neurons in the neighborhood of CHC.1 and CHC.2 cells were mostly L4 and L4/5 subclasses, whereas those in the neighborhood of CHC.3 were mostly L2/3 subclass (Figure S5K). Thus, distinct chandelier cells are involved in forming local circuits and modulating neuronal activity of different glutamatergic types.

The balance between output-controlling PV and input-controlling SST GABAergic neurons contributes to regional differences in local circuit properties.[43] We therefore examined L2/3 PV/ (PV + SST) cell density ratios and found that PV/(PV + SST) density ratio was the highest in motor cortices (F1–F3, F6, and F7) and the entorhinal area and the lowest in the insular and auditory cortices (Figure 5I). Previous studies in mouse suggested areal hierarchy in relative density between PV and SST neurons.[43] However, PV and SST density ratio in macaque did not show any significant correlation with the hierarchical levels in either sensory system (Figure S5L). To investigate the correlation between hierarchical level and PV/SST cell-type compositions in the monkey cortex, we performed principal component analysis (PCA) on the cell composition vector (the relative density of all PV and SST cell types) in each cortical region. The first principal component (PC1) of various regions exhibited a positive correla-

tion with the hierarchical levels of both sensory systems (Figure 5J), suggesting that the PV and SST interneurons with distinct soma- and dendritic-targeting properties are tightly regulated to support the functions of various cortical regions. Further examination of the cell types contributing significantly to the PC1 revealed that PV.9 POSTN/ADAMTS20, SST.28 TRPC6/PLSCR5, and PV.12 POSTN/LRIG3 were enriched in regions of high hierarchical levels, whereas SST.18 ADAMTS6/ESM1, SST.9 SYTL5/ADAMTS6, and PV.5 POSTN/SULF1 were enriched in regions of low hierarchical levels (Figure S5M). In addition, we found significant correlation between the gene expression of neurotransmitter and neuromodulator receptors in PV/SST neurons and hierarchical levels in both sensory systems (Figure 5K). Thus, both cell density and receptors expressed in PV and SST cells are tightly regulated in a manner dependent on hierarchy in the monkey cortex.

Spatial organization of non-neuronal cells

Using snRNA-seq data, we identified 34 non-neuronal cell types that belonged to 6 subclasses, ASC, OLG, OPC, MG, EC, and VMLC, identified by various conventional marker genes (Figure S6A). These non-neuronal cell types also showed preferential laminar localization across cortical regions (Figure 6A). For examples, EC and VLMC cell types were predominantly distributed in L1, OLG cells were enriched in L6, and ASCs were dispersed throughout cortical layers (Figure 6A). Consistent with previous reports,[44] glutamate transporters (SLC1A2 and SLC1A3) and GABA transporters (SLC6A11 and SLC6A1) were highly expressed in almost all ASC types (Figure S6A). Notably, we also identified two groups of ASCs, group 1 (ASC.1 GFAP/APLNR and ASC.2 MSX2/TFAP2C) and group 2 (ASC.11 ADGRV1/GRAMD2), which were predominantly located in L1 and L6, respectively (Figures 6B and S6B). These two groups expressed different sets of genes (GFAP, SOX6, MSX1, and PAX6 in group 1; GRIN2A, GRIN2B, GRIN1, GRIA2, GRIA3, and GRIA4 in group 2) related to distinct GO terms (Figures 6C and S6C–S6E). Further analysis revealed that the glutamatergic receptor genes, including AMPA, Kainate, NMDA, and Delta families, were all expressed at a higher level in the group 2 ASCs (Figure 6D). Thus, specific ASC types with different localization may serve distinct cortical functions in the macaque brain.

In addition to the laminar preference, we also observed that L6-enriched ASCs were more abundant in V1 than in prefrontal cortex (PFC) (Figure 6B). Systematic evaluation of the regional distribution of non-neuronal cell types showed that ASC, MG,

---

Figure 4. Layer and regional preferences of glutamatergic cell types

(A) Volume-normalized cortical layer distribution (top), relative percentage among nine cortical lobes (middle), and regional distribution entropy (below) of each glutamatergic cell type across the macaque cortex.

(B) Spatial distribution of all glutamatergic cell types along the A-P axis (EBZ coordinates).

(C and D) Distribution density (C) and images (D) of example glutamatergic cell types with distinct regional localization in V1, F1, and temporal pole at similar coronal coordinates from three monkeys.

(E) Dot plot showing the expression patterns of top marker genes for the region-specific cell types in (D).

(F) Spatial expression pattern of the indicated marker genes for the region-specific cell types in (D).

(G) RNAscope assay of NTNG1 in V1.

(H) Schematics showing the procedure of neighborhood composition analysis.

(I) UMAP of the neighborhood composition of the region-specific cell types shown in (C).

(J) Expression levels of AMPA, NMDA, and metabotropic glutamate receptor subunit genes in different layers along the hierarchical level in visual systems.

See also Figure S4 and Table S5.
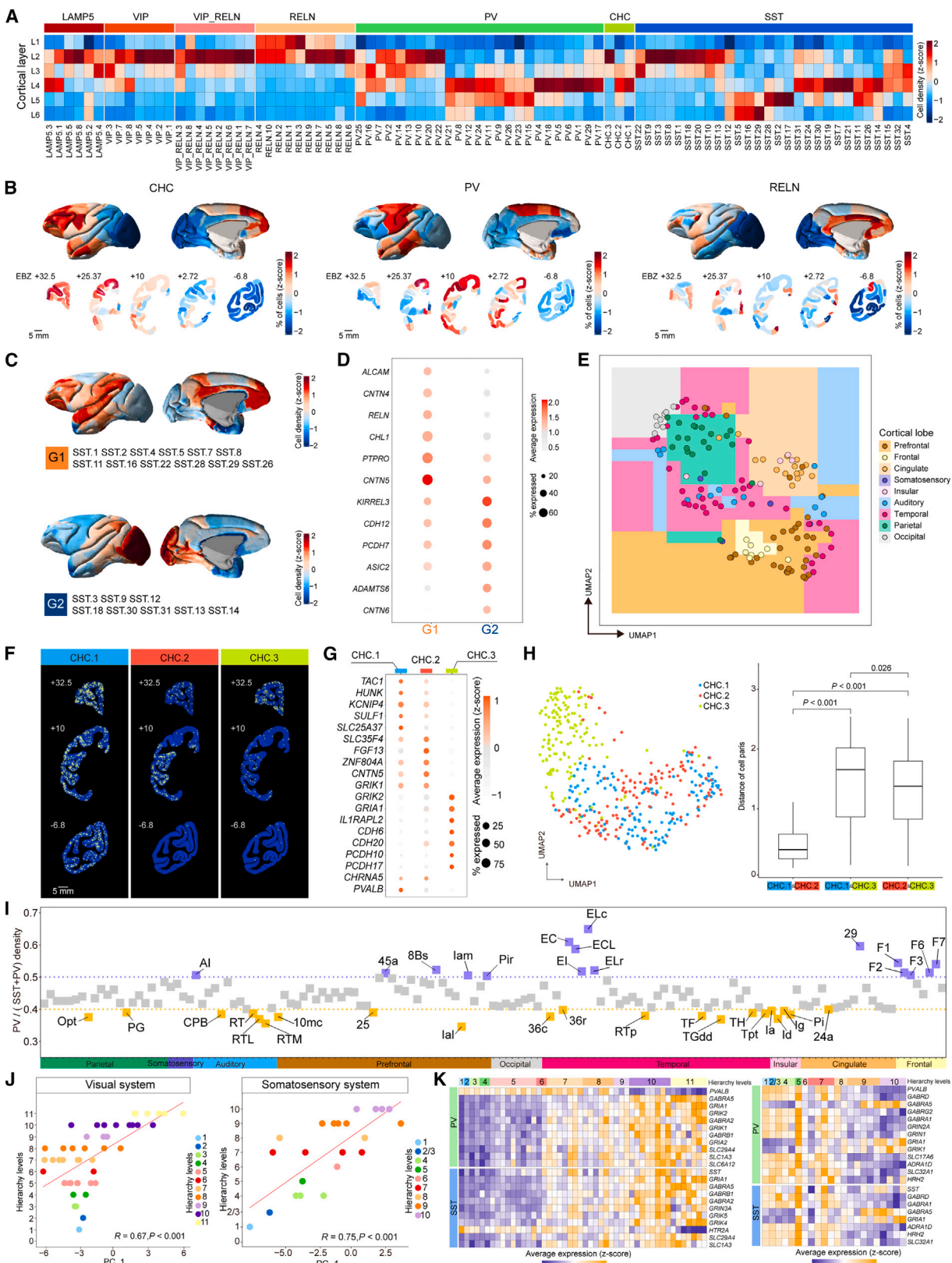
(legend on next page)

and OLG cell types were distributed in a gradient along the A-P axis (Figure 6E; Table S5). Among ASC cell types, ASC.10, ASC.11, ASC.13, and ASC.16 were preferentially enriched in the occipital lobe. By contrast, ASC.2, ASC.8, ASC.9, and ASC.12 were preferentially located in the prefrontal and temporal lobes (Figure 6F). For MG cell types, we found that deep-layer-enriched MG.1 *CX3CR1/CLEC12A* and superficial-layer-enriched MG.2 *CD5L/CCL13* were also enriched in anterior and posterior regions, respectively (Figure 6A and 6E).

For OPC and OLG cell types, we performed pseudo-time analysis of snRNA-seq data and found a lineage trajectory from OPCs to mature OLGs (Figures S6F–S6H), consistent with previous reports in mouse and human.[35,45] Furthermore, stereo-seq data showed that OLGs were enriched in L6, whereas OPCs (highly expressing *PDGFRA* and *COL9A1*) were mostly found in L1 and L2 (Figure 6A). In addition, OPCs were widely distributed along the A-P axis and across cortical regions (Figures 6E and 6F). Among OLG cell types, we identified two groups based on their global distribution: group 1 cells (OLG.3 *ANLN/CNDP1*, OLG.5 *PLP1/ERMN*, OLG.7 *ANLN/MOBP*, and OLG.8 *PLP1/OPALIN*) and group 2 cells (OLG.6 *PLP1/MOG* and OLG.11 *ANLN/MOG*) were localized to medial and posterior regions along the A-P axis, respectively (Figure 6E). Notably, among group 1 OLG cells, OLG.7 *ANLN/MOBP* cell type showed distinct localization in F1 region (Figures 6G and S6I), as further confirmed by high expression levels of its marker genes in F1 across coronal sections (Figures 6H and S6I). Perineuronal OLGs provide metabolic support to neurons,[46] the F1-enriched OLG cell type may serve for the higher energy demands of neuronal firing in the F1 region of the macaque brain. The two OLG groups also showed differential gene expression patterns (*PLP1*, *CNP*, and *TF* in group 1; *NRXN1*, *NRXN3*, and *GRIK2* in group 2; Figure 6I). Taken together, these results regarding the spatial distribution of various non-neuronal cell types and their marker genes suggested distinct laminar- and region-specific functions of these non-neuronal cell types in the monkey cortex.

Primate-specific cell types

Neocortex enlargement during evolution is a critical step for the emergence of higher cognitive functions in primates.[11,47] To explore whether new cell types appear in the primate cortex, we compared our macaque single-nucleus transcriptome data on the prefrontal, motor, and visual cortices with those retrieved from published studies on both the human and mouse cortices.[12,16,48,49] We first focused on single-cell datasets of glutamatergic neurons across species in each of the three cortices and identified 8 glutamatergic cell subclasses (Car3, L2/3 IT, L4/5 IT, L5 PT, L5/6 IT, L5/6 NP, L6 CT, and L6b) based on canonical marker genes (Figures 7A–7C). Cross-species comparison showed that macaques shared a larger number of marker genes for each subclass with humans than with mice (Figure S7A). Species-specific expression of a total of 1,630 genes was found for all 8 cell subclasses among human, macaque, and mouse, but conserved expression among all species was identified for only 201 genes in the prefrontal cortex (Figure S7B), consistent with previous findings based on single-cell RNA-seq analyses.[12,15,35] Although these glutamatergic cell subclasses were consistent across species, a group of L4/5 IT neurons presented in all three cortical regions (PFC, M1, and V1) was found in macaques and humans, but not in mice (Figures 7A–7C and S7C). Remarkably, a pairwise comparison of the transcriptome profiles of cell types uncovered six glutamatergic L4 cell types that were present in the PFC, F1, and V1 regions of macaques and humans but not in mice (Figures 7A–7C, marked in red). Spatial transcriptome map showed that these cell types were preferentially distributed in L4 of most cortical regions (Figure 7D). Further cross-species comparison analysis using cells only from the medial and orbital prefrontal cortices also revealed the existence of primate-specific L4 cell types (Figures S7D–S7F). These primate-specific cell types showed higher abundance in the 46 and 10 regions of the macaque prefrontal cortex (Figure S7G), suggesting that primate-specific cell types might be associated with the emergence of new cortical regions in primates. Cross-species comparison of GABAergic and non-neuronal cell types revealed the similarity of cell types in these cortical regions between primates and mice (Figure S7H).

To characterize the molecular fingerprints of primate-specific L4 glutamatergic types, we conducted differential expression analysis and found 226 highly expressed genes in the 6 primate-specific cell types (Figure 7E). Further GO analysis revealed that these genes were associated with axonogenesis and synapse organization (Figure 7F). These genes also included L4/5 marker genes, such as *RORB*, *IL1RAPL2*, and *TSHZ2*, top-ranked genes in these primate-specific cell types (Figure 7E). In addition, we found that 53 out of the 226 genes, including *FOXP2*, *EPHA3*, and *DCC*, showed much higher expression levels in the L4/5 IT subclass

---

Figure 5. Organization of GABAergic cell types

(A) Heatmap of volume-normalized cortical layer distribution of GABAergic cell types.

(B) Spatial distribution (upper, 3D rendering) and 2D plot (lower) of 3 major GABAergic subclasses along the A-P axis.

(C) Side and medial views of the 3D visualization of two SST cell groups.

(D) Dot plot showing the expression of enriched genes in G1 and G2 SST groups.

(E) UMAP clustering of SST cell-type compositions.

(F) Distribution images showing three CHC types.

(G) Dot plot showing the expression patterns of various marker genes for the three CHC types in (F).

(H) Left: UMAP based on the neighborhood compositions of glutamatergic neurons adjacent to three CHC cell types. Right: average UMAP distance of each cell pair between CHC types.

(I) Relative density of PV vs. SST cell types in various cortical regions.

(J) Correlation between PC1 of PV and SST cell-composition vectors and regional hierarchy levels.

(K) Expression levels of neurotransmitter and neuromodulator receptor subunit and transporter genes in PV or SST neurons along the hierarchical level in visual (left) and somatosensory (right) systems.

See also Figure S5 and Tables S5 and S6.
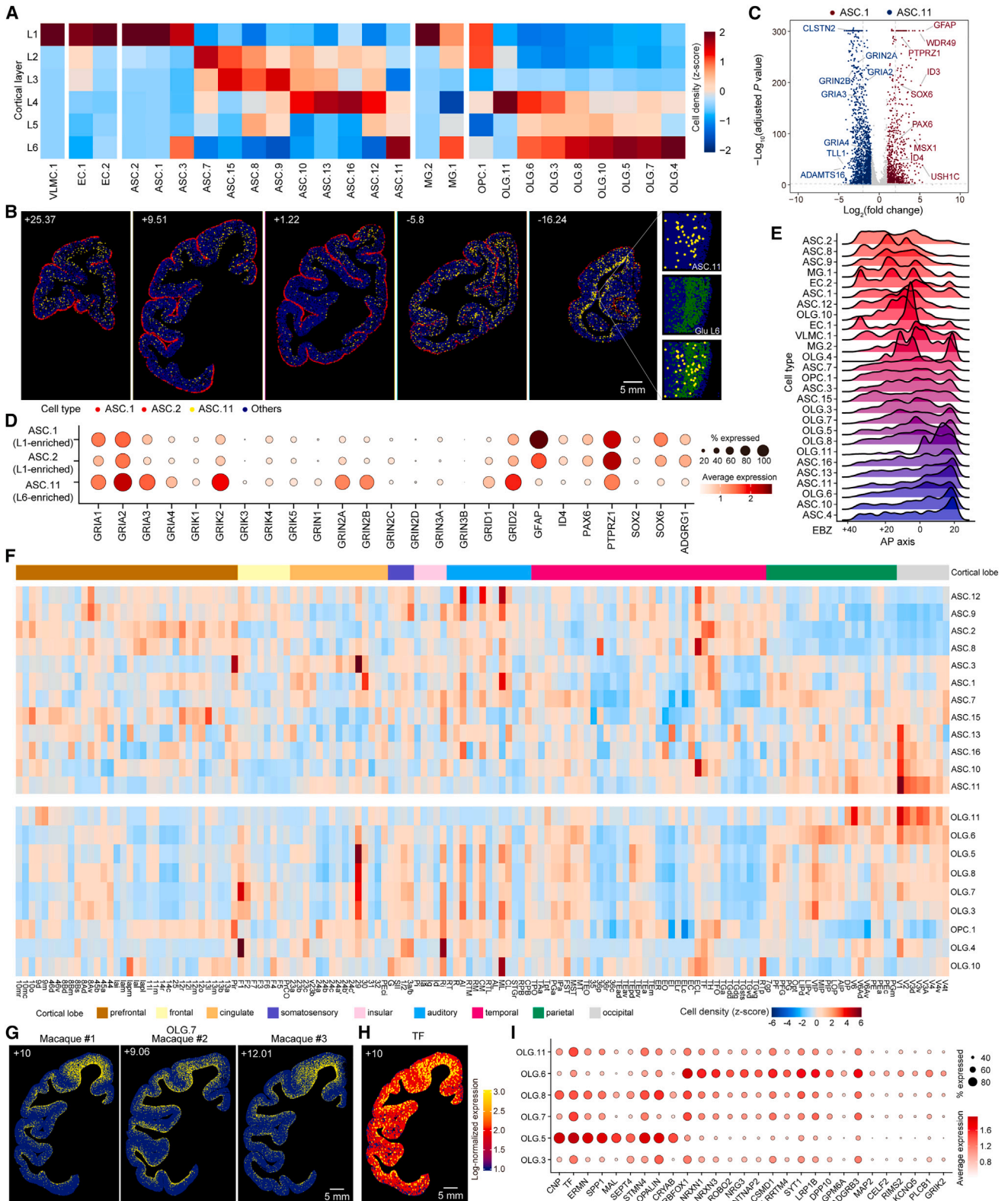
(legend on next page)

neurons of humans and macaques than in those of mice (Figure 7G). Of particular interest is *FOXP2*, which encodes a transcription factor involved in developmental verbal dyspraxia.[50] We further quantified *FOXP2* expression in each cortical layer of all regions of the macaque cortex and found that this gene showed the highest expression level in L4 for most cortical regions (Figure 7H). However, for regions exhibiting no clear L4, such as frontal and entorhinal cortices, *FOXP2* expression was highest in L6 (Figure 7H), consistent with a recent study showing the primate-specific expression of *FOXP2* at L4 in PFC.[35] Similar high expression of *EPHA3* and *DCC* was also found in L4 of macaque and humans (Figures 7G and 7H). For cortical regions without clear L4, *EPHA3* and *DCC* showed the highest expression levels in L2/3 and L5/6, respectively (Figure 7H). Our RNAscope assays validated the highest expression levels of *FOXP2* and *EPHA3* in L4 of V2, whereas in the V1 region, *FOXP2* and *EPHA3* showed the highest expression levels in L6 and L2/3/5, respectively (Figure 7I). Consistently, previous *in situ* hybridization (ISH) studies also showed the region-dependent laminar expression of these genes in humans (https://human.brain-map.org/ish/specimen/show/78721333?gene=60634). By contrast, ISH data revealed that *FOXP2* was only expressed in L6 of mice (https://mouse.brain-map.org/experiment/show/72079884). Thus, the evolutionary expansion of primate cortex was accompanied by the emergence of primate-specific cell types located in L4 and distinct laminar gene expression patterns in a region-dependent manner.

DISCUSSION

In this study, we have performed a comprehensive spatial transcriptome analysis of the entire macaque monkey cortex with single-cell resolution, using a recently developed stereo-seq technology. Our brain-wide transcriptome analysis was based on 161 coronal sections across the left hemisphere of three male macaque brains. The reproducibility of our data was confirmed by gene profiles and cell compositions mapped in sections of similar coronal coordinates from three monkeys. Our interactive web portal offers a useful resource for the research community.

The discovery of a large number of transcriptome-defined cell types within glutamatergic and GABAergic neurons raises the question of their relationship with cell types defined by dendritic morphology,[51–53] electrophysiological properties,[51,54,55] and single-cell connectome.[37,56–58] The integration of cell types defined by various approaches represents an important issue to be addressed,[58] as illustrated by recent studies in mice[51,54,59,60] and humans.[11,61] The diversity of cell types based on gene expression profiles is bound to be reflected in the diverse cellular structure and function. In particular, we found the L2/3 glutamatergic cells highly expressed *ADCYAP1*, a gene encoding pituitary adenylate-cyclase-activating polypeptide (PACAP), a peptide that drives cAMP signaling and serves as the "master regulator" of stress signaling in the nervous system. It is known that *ADCYAP1* is enriched in the L3 pyramidal cells of the rhesus monkey dorsolateral prefrontal cortex (dlPFC), based on laser capture microdissection.[62] Such layer-specific expression of genes across various regions of the cortex calls for further studies on their roles in cortical processing. It is noteworthy that we found regional variations in the trends of parvalbumin and calretinin neurons between our datasets and those previously reported using immunohistochemistry staining data[63] (data not shown), which might be explained by the discrepancies between RNA and protein levels within cells.[64–67]

Notably, our study revealed several rules of cellular organization with respect to cortical hierarchy. First, all three major cell classes contain cell types with their regional densities positively or negatively correlated with the cortical hierarchy of the visual and somatosensory systems. Second, many cell types showing positive or negative correlation with hierarchy are shared by these sensory systems. Third, the number of glutamatergic cell types with negative correlation with hierarchy is much higher than that of GABAergic cell types. Finally, the regional distribution of non-neuronal cell types only exhibits positive correlations with the hierarchy level. These organization rules on cell-type distribution may underlie the increasing complexity of information processing with the hierarchy level and provide the basis for further studying the specific roles of various cell types in cortical functions at different hierarchy levels. Furthermore, the increased expression of the glutamatergic receptor genes and the decreasing density of various glutamatergic cell types along the hierarchy level imply that the expression of these genes is increasingly elevated in each cell with its hierarchy level, consistent with the elevated spine density in neurons.[68]

Neocortical expansion in prefrontal, parietal, and temporal cortices is an important step in primate evolution,[69] and it is likely to involve primate-specific gene expression patterns that underlie more complex cognitive functions. The primate brain is more hierarchically organized than the mouse brain.[70,71] The primate-specific L4 cell types found in this study highly expressed the neuropsychiatric risk gene *FOXP2*, ephrin receptor *EPHA3*, and neurodevelopment-related gene *DCC*. Further comparison of spatial transcriptomic maps among humans, non-human primates, and rodents will provide molecular insights into the evolution and morphogenesis of the primate brain.

Figure 6. Distribution of non-neuronal cell types
(A) Heatmap of the volume-normalized cell density of non-neuronal cell types.
(B) Spatial distribution of ASC types in 5 representative cortical sections.
(C) Volcano plot showing DEG levels in L1- and L6-enriched ASC types.
(D) Dot plot showing the gene expression patterns of 3 layer-specific ASC types.
(E) Density profiles of various non-neuronal cell types along the A-P axis.
(F) Heatmap showing the distribution of ASC and OLG cell types across cortical regions.
(G and H) Images showing the distribution of F1-enriched OLG.7 (G) and marker gene (H) in representative sections.
(I) Expression patterns of the indicated genes in various OLG types.
See also Figure S6 and Table S5.
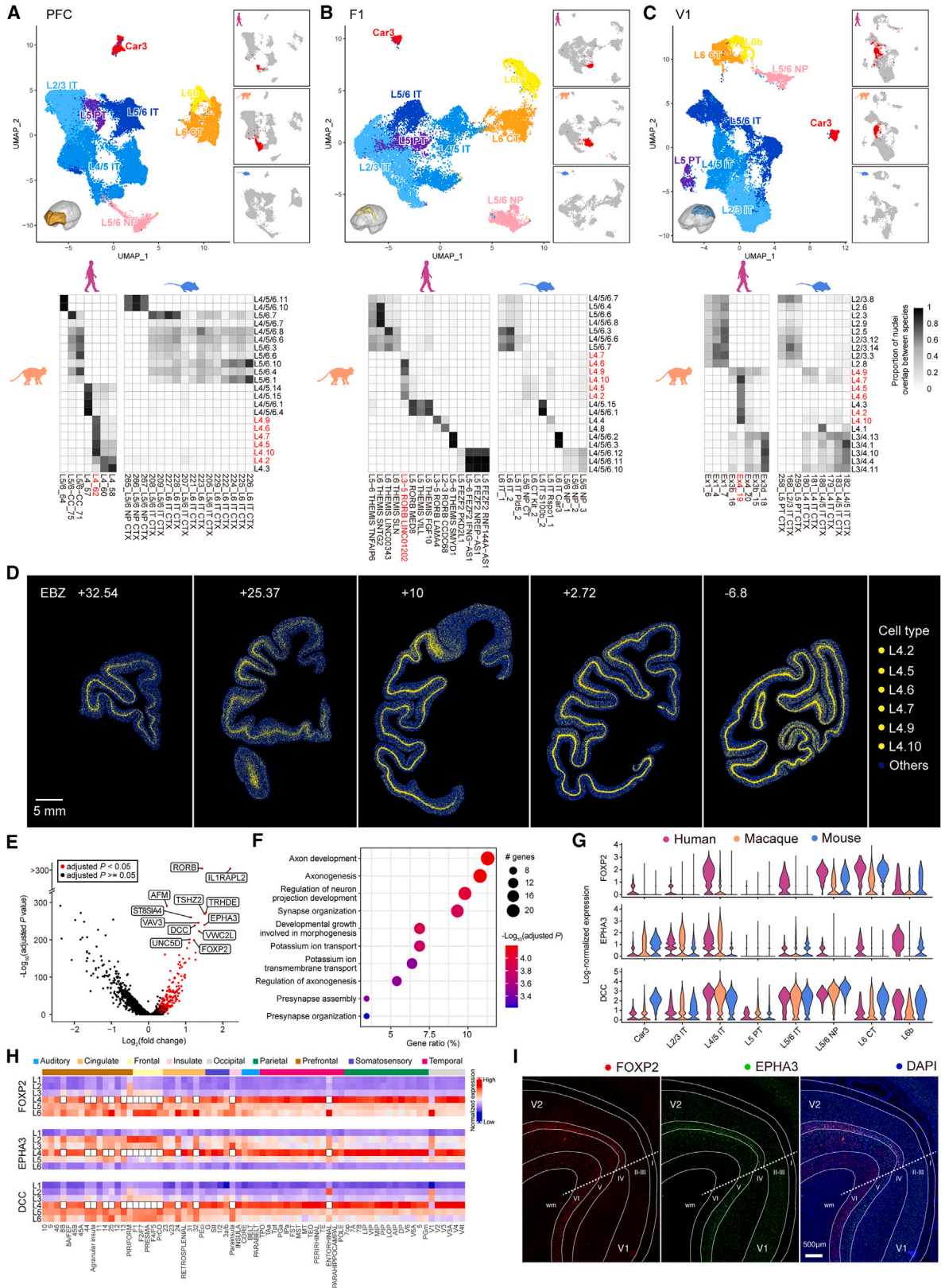
(legend on next page)

As macaque models of brain disorders are now becoming available,[72] spatial transcriptomic analysis of these models will help elucidate pathogenic mechanisms and identify therapeutic targets for human brain disorders. Our results provide the first comprehensive brain-wide spatial transcriptome of the macaque cortex at the single-cell level and pave the way for future molecular and cellular studies of brain organization during evolution, development, aging, and pathogenesis.

Limitations of the study

The average number of genes captured per cell (∼500) by the present method was higher than that found by using previously reported methods,[28] although it remained much lower than that obtained by conventional snRNA-seq method. We have partially circumvented the problem by using our snRNA-seq data to assist cell-type identification. Technical improvement in the mRNA-capturing capability and combination with protein recognition may further elevate the sensitivity and precision of the spatial-resolved cell taxonomy in the brain. The 3D spatial transcriptome atlas at the single-cell resolution was based on a total of 119 coronal sections with 500-μm spacing profiled in this study covering all macaque cortical regions, which could be extended to whole brain by adding sagittal sections. In addition, only male monkeys were used in this study, and the sexual dimorphism of the gene expression patterns of the macaque brain needs to be examined in the future.

STAR★METHODS

Detailed methods are provided in the online version of this paper and include the following:

- KEY RESOURCES TABLE
- RESOURCE AVAILABILITY
  - Lead contact
  - Materials availability
  - Data and code availability
- EXPERIMENTAL MODEL AND STUDY PARTICIPANT DETAILS
  - Animal care
- METHOD DETAILS
  - Tissue collection
  - Tissue cryosection and section flattening
  - Tissue-section processing for stereo-seq
  - Library preparation and sequencing
  - Immunohistochemical staining
  - RNA in situ hybridization (RNAscope)
  - Brain tissue collection for snRNA-seq

- Single-nucleus suspension preparation
- snRNA-seq library construction and sequencing
- snRNA-seq data processing
- Cell clustering and cell-type identification using snRNA-seq data
- Prediction of the projection properties of glutamatergic cell subclasses
- Stereo-seq data processing
- Image-based single-cell segmentation of stereo-seq data
- Cortical region and layer parcellation
- Stereo-seq data preprocessing
- Cell-type annotation of single cells in the stereo-seq map
- Quantification of spatial distribution of various cell types in the stereo-seq map
- Correspondence of cell types between stereo-seq and snRNA-seq data
- Neighborhood complexity
- Region-specific cell types
- Correlation of cell-type distribution with cortical hierarchy levels
- Spatial distribution of neurotransmitter and neuromodulator receptor genes
- Calculation of glutamatergic neuron neighbor of CHC subpopulations in different cortical regions
- Comparison of layer-specific astrocytes
- Pseudotime trajectory analysis of oligodendrocyte lineage
- Reconstruction of the 3D cell atlas
- Cross-species analysis of different cell types
- QUANTIFICATION AND STATISTICAL ANALYSIS

SUPPLEMENTAL INFORMATION

Supplemental information can be found online at https://doi.org/10.1016/j.cell.2023.06.009.

Figure 7. Primate-specific cell types

(A–C) UMAP of integrated snRNA-seq/scRNA-seq data for PFC (A), F1 (B), and V1 (C) from three species. Lower panels depict the species comparison of glutamatergic cell types.

(D) Spatial distribution of 6 primate-specific glutamatergic cell types in 5 representative coronal sections.

(E) Volcano plot of DEGs between primate-specific and other cell types.

(F) GO terms associated with genes highly expressed in primate-specific cell types.

(G) Violin plot showing the expression levels of 3 example genes across species.

(H) Layer distribution of *FOXP2*, *EPHA3*, and *DCC* of various cortical regions. White squares mark brain regions with no apparent layer 4.

(I) RNAscope assay showing the layer distribution of *FOXP2* and *EPHA3*.

See also Figure S7 and Table S7.

REFERENCES

1. Sousa, A.M.M., Meyer, K.A., Santpere, G., Gulden, F.O., and Sestan, N. (2017). Evolution of the human nervous system function, structure, and development. Cell 170, 226–247. https://doi.org/10.1016/j.cell.2017.06.036.

2. Bakken, T.E., Miller, J.A., Ding, S.L., Sunkin, S.M., Smith, K.A., Ng, L., Szafer, A., Dalley, R.A., Royall, J.J., Lemon, T., et al. (2016). A comprehensive transcriptional map of primate brain development. Nature 535, 367–375. https://doi.org/10.1038/nature18637.

3. Lein, E., Borm, L.E., and Linnarsson, S. (2017). The promise of spatial transcriptomics for neuroscience in the era of molecular cell typing. Science 358, 64–69. https://doi.org/10.1126/science.aan6827.

4. Bernard, A., Lubbers, L.S., Tanis, K.Q., Luo, R., Podtelezhnikov, A.A., Finney, E.M., McWhorter, M.M., Serikawa, K., Lemon, T., Morgan, R., et al. (2012). Transcriptional architecture of the primate neocortex. Neuron 73, 1083–1099. https://doi.org/10.1016/j.neuron.2012.03.002.

5. He, Z., Han, D., Efimova, O., Guijarro, P., Yu, Q., Oleksiak, A., Jiang, S., Anokhin, K., Velichkovsky, B., Grünewald, S., and Khaitovich, P. (2017). Comprehensive transcriptome analysis of neocortical layers in humans, chimpanzees and macaques. Nat. Neurosci. 20, 886–895. https://doi.org/10.1038/nn.4548.

6. Maynard, K.R., Collado-Torres, L., Weber, L.M., Uytingco, C., Barry, B.K., Williams, S.R., Catallini, J.L., 2nd, Tran, M.N., Besich, Z., Tippani, M., et al. (2021). Transcriptome-scale spatial gene expression in the human dorsolateral prefrontal cortex. Nat. Neurosci. 24, 425–436. https://doi.org/10.1038/s41593-020-00787-0.

7. Markov, N.T., Ercsey-Ravasz, M., Van Essen, D.C., Knoblauch, K., Toroczkai, Z., and Kennedy, H. (2013). Cortical high-density counterstream architectures. Science 342, 1238406. https://doi.org/10.1126/science.1238406.

8. Zhu, Y., Sousa, A.M.M., Gao, T., Skarica, M., Li, M., Santpere, G., Esteller-Cucala, P., Juan, D., Ferrández-Peral, L., Gulden, F.O., et al. (2018). Spatiotemporal transcriptomic divergence across human and macaque brain development. Science 362, eaat8077. https://doi.org/10.1126/science.aat8077.

9. Khrameeva, E., Kurochkin, I., Han, D., Guijarro, P., Kanton, S., Santel, M., Qian, Z., Rong, S., Mazin, P., Sabirov, M., et al. (2020). Single-cell-resolution transcriptome map of human, chimpanzee, bonobo, and macaque brains. Genome Res. 30, 776–789. https://doi.org/10.1101/gr.256958.119.

10. Krienen, F.M., Goldman, M., Zhang, Q., C H Del Rosario, R., Florio, M., Machold, R., Saunders, A., Levandowski, K., Zaniewski, H., Schuman, B., et al. (2020). Innovations present in the primate interneuron repertoire. Nature 586, 262–269. https://doi.org/10.1038/s41586-020-2781-z.

11. Berg, J., Sorensen, S.A., Ting, J.T., Miller, J.A., Chartrand, T., Buchin, A., Bakken, T.E., Budzillo, A., Dee, N., Ding, S.L., et al. (2021). Human neocortical expansion involves glutamatergic neuron diversification. Nature 598, 151–158. https://doi.org/10.1038/s41586-021-03813-8.

12. Bakken, T.E., Jorstad, N.L., Hu, Q., Lake, B.B., Tian, W., Kalmbach, B.E., Crow, M., Hodge, R.D., Krienen, F.M., Sorensen, S.A., et al. (2021). Comparative cellular analysis of motor cortex in human, marmoset and mouse. Nature 598, 111–119. https://doi.org/10.1038/s41586-021-03465-8.

13. BRAIN Initiative Cell Census Network (BICCN) (2021). A multimodal cell census and atlas of the mammalian primary motor cortex. Nature 598, 86–102. https://doi.org/10.1038/s41586-021-03950-0.

14. Yao, Z., Liu, H., Xie, F., Fischer, S., Adkins, R.S., Aldridge, A.I., Ament, S.A., Bartlett, A., Behrens, M.M., Van den Berge, K., et al. (2021). A transcriptomic and epigenomic cell atlas of the mouse primary motor cortex. Nature 598, 103–110. https://doi.org/10.1038/s41586-021-03500-8.

15. Hodge, R.D., Bakken, T.E., Miller, J.A., Smith, K.A., Barkan, E.R., Graybuck, L.T., Close, J.L., Long, B., Johansen, N., Penn, O., et al. (2019). Conserved cell types with divergent features in human versus mouse cortex. Nature 573, 61–68. https://doi.org/10.1038/s41586-019-1506-7.

16. Yao, Z., van Velthoven, C.T.J., Nguyen, T.N., Goldy, J., Sedeno-Cortes, A.E., Baftizadeh, F., Bertagnolli, D., Casper, T., Chiang, M., Crichton, K., et al. (2021). A taxonomy of transcriptomic cell types across the isocortex and hippocampal formation. Cell 184, 3222–3241.e26. https://doi.org/10.1016/j.cell.2021.04.021.

17. Lui, J.H., Nguyen, N.D., Grutzner, S.M., Darmanis, S., Peixoto, D., Wagner, M.J., Allen, W.E., Kebschull, J.M., Richman, E.B., Ren, J., et al. (2021). Differential encoding in prefrontal cortex projection neuron classes across cognitive tasks. Cell 184, 489–506.e26. https://doi.org/10.1016/j.cell.2020.11.046.

18. Aldinger, K.A., Thomson, Z., Phelps, I.G., Haldipur, P., Deng, M., Timms, A.E., Hirano, M., Santpere, G., Roco, C., Rosenberg, A.B., et al. (2021). Spatial and cell type transcriptional landscape of human cerebellar development. Nat. Neurosci. 24, 1163–1175. https://doi.org/10.1038/s41593-021-00872-y.

19. Chen, K.H., Boettiger, A.N., Moffitt, J.R., Wang, S., and Zhuang, X. (2015). RNA imaging. Spatially resolved, highly multiplexed RNA profiling in single cells. Science 348, aaa6090. https://doi.org/10.1126/science.aaa6090.

20. Eng, C.L., Lawson, M., Zhu, Q., Dries, R., Koulena, N., Takei, Y., Yun, J., Cronin, C., Karp, C., Yuan, G.C., et al. (2019). Transcriptome-scale super-resolved imaging in tissues by RNA seqFISH. Nature 568, 235–239. https://doi.org/10.1038/s41586-019-1049-y.

21. Lee, J.H., Daugharthy, E.R., Scheiman, J., Kalhor, R., Yang, J.L., Ferrante, T.C., Terry, R., Jeanty, S.S., Li, C., Amamoto, R., et al. (2014). Highly multiplexed subcellular RNA sequencing in situ. Science 343, 1360–1363. https://doi.org/10.1126/science.1250212.

22. Wang, X., Allen, W.E., Wright, M.A., Sylwestrak, E.L., Samusik, N., Vesuna, S., Evans, K., Liu, C., Ramakrishnan, C., Liu, J., et al. (2018). Three-dimensional intact-tissue sequencing of single-cell transcriptional states. Science 361, eaat5691. https://doi.org/10.1126/science.aat5691.

23. Rodriques, S.G., Stickels, R.R., Goeva, A., Martin, C.A., Murray, E., Vanderburg, C.R., Welch, J., Chen, L.M., Chen, F., and Macosko, E.Z. (2019). Slide-seq: A scalable technology for measuring genome-wide expression at high spatial resolution. Science 363, 1463–1467. https://doi.org/10.1126/science.aaw1219.

24. Ståhl, P.L., Salmén, F., Vickovic, S., Lundmark, A., Navarro, J.F., Magnusson, J., Giacomello, S., Asp, M., Westholm, J.O., Huss, M., et al. (2016). Visualization and analysis of gene expression in tissue sections by spatial transcriptomics. Science 353, 78–82. https://doi.org/10.1126/science.aaf2403.

25. Stickels, R.R., Murray, E., Kumar, P., Li, J., Marshall, J.L., Di Bella, D.J., Arlotta, P., Macosko, E.Z., and Chen, F. (2021). Highly sensitive spatial transcriptomics at near-cellular resolution with Slide-seqV2. Nat. Biotechnol. 39, 313–319. https://doi.org/10.1038/s41587-020-0739-1.

26. Vickovic, S., Eraslan, G., Salmén, F., Klughammer, J., Stenbeck, L., Schapiro, D., Äijö, T., Bonneau, R., Bergenstråhle, L., Navarro, J.F., et al. (2019). High-definition spatial transcriptomics for in situ tissue profiling. Nat. Methods 16, 987–990. https://doi.org/10.1038/s41592-019-0548-y.

27. Liu, Y., Yang, M., Deng, Y., Su, G., Enninful, A., Guo, C.C., Tebaldi, T., Zhang, D., Kim, D., Bai, Z., et al. (2020). High-spatial-resolution multiomics sequencing via deterministic barcoding in tissue. Cell 183, 1665–1681.e18. https://doi.org/10.1016/j.cell.2020.10.026.

28. Chen, A., Liao, S., Cheng, M., Ma, K., Wu, L., Lai, Y., Qiu, X., Yang, J., Xu, J., Hao, S., et al. (2022). Spatiotemporal transcriptomic atlas of mouse organogenesis using DNA nanoball-patterned arrays. Cell 185, 1777–1792.e21. https://doi.org/10.1016/j.cell.2022.04.003.

29. Liu, C., Wu, T., Fan, F., Liu, Y., Wu, L., Junkin, M., Wang, Z., Yu, Y., Wang, W., Wei, W., et al. (2019). A portable and cost-effective microfluidic system for massively parallel single-cell transcriptome profiling https://doi.org/10.1101/818450.

30. Han, L., Wei, X., Liu, C., Volpe, G., Zhuang, Z., Zou, X., Wang, Z., Pan, T., Yuan, Y., Zhang, X., et al. (2022). Cell transcriptomic atlas of the non-human primate Macaca fascicularis. Nature 604, 723–731. https://doi.org/10.1038/s41586-022-04587-3.

31. Shen, R., Liu, L., Wu, Z., Zhang, Y., Yuan, Z., Guo, J., Yang, F., Zhang, C., Chen, B., Feng, W., et al. (2022). Spatial-ID: a cell typing method for spatially resolved transcriptomics via transfer learning and spatial embedding. Nat. Commun. 13, 7640. https://doi.org/10.1038/s41467-022-35288-0.

32. Song, S., Sjöström, P.J., Reigl, M., Nelson, S., and Chklovskii, D.B. (2005). Highly nonrandom features of synaptic connectivity in local cortical circuits. PLoS Biol. 3, e68. https://doi.org/10.1371/journal.pbio.0030068.

33. Perin, R., Berger, T.K., and Markram, H. (2011). A synaptic organizing principle for cortical neuronal groups. Proc. Natl. Acad. Sci. USA 108, 5419–5424. https://doi.org/10.1073/pnas.1016051108.

34. Felleman, D.J., and Van Essen, D.C. (1991). Distributed hierarchical processing in the primate cerebral cortex. Cereb. Cortex 1, 1–47. https://doi.org/10.1093/cercor/1.1.1-a.

35. Ma, S., Skarica, M., Li, Q., Xu, C., Risgaard, R.D., Tebbenkamp, A.T.N., Mato-Blanco, X., Kovner, R., Krsnik, Ž., de Martin, X., et al. (2022). Molecular and cellular evolution of the primate dorsolateral prefrontal cortex. Science 377, eabo7257. https://doi.org/10.1126/science.abo7257.

36. Fang, R., Xia, C., Close, J.L., Zhang, M., He, J., Huang, Z., Halpern, A.R., Long, B., Miller, J.A., Lein, E.S., and Zhuang, X. (2022). Conservation and divergence of cortical cell organization in human and mouse revealed by MERFISH. Science 377, 56–62. https://doi.org/10.1126/science.abm1741.

37. Tasic, B., Yao, Z., Graybuck, L.T., Smith, K.A., Nguyen, T.N., Bertagnolli, D., Goldy, J., Garren, E., Economo, M.N., Viswanathan, S., et al. (2018). Shared and distinct transcriptomic cell types across neocortical areas. Nature 563, 72–78. https://doi.org/10.1038/s41586-018-0654-5.

38. Wilcox, J.A., and Quadri, S. (2014). Replication of NTNG1 association in schizophrenia. Psychiatr. Genet. 24, 266–268. https://doi.org/10.1097/YPG.0000000000000061.

39. Arnsten, A.F., and Wang, M. (2016). Targeting prefrontal cortical systems for drug development: potential therapies for cognitive disorders. Annu. Rev. Pharmacol. Toxicol. 56, 339–360. https://doi.org/10.1146/annurev-pharmtox-010715-103617.

40. Burt, J.B., Demirtaş, M., Eckner, W.J., Navejar, N.M., Ji, J.L., Martin, W.J., Bernacchia, A., Anticevic, A., and Murray, J.D. (2018). Hierarchy of transcriptomic specialization across human cortex captured by structural neuroimaging topography. Nat. Neurosci. 21, 1251–1259. https://doi.org/10.1038/s41593-018-0195-0.

41. Inda, M.C., Defelipe, J., and Muñoz, A. (2007). The distribution of chandelier cell axon terminals that express the GABA plasma membrane transporter GAT-1 in the human neocortex. Cereb. Cortex 17, 2060–2071. https://doi.org/10.1093/cercor/bhl114.

42. Blazquez-Llorca, L., Woodruff, A., Inan, M., Anderson, S.A., Yuste, R., DeFelipe, J., and Merchan-Perez, A. (2015). Spatial distribution of neurons innervated by chandelier cells. Brain Struct. Funct. 220, 2817–2834. https://doi.org/10.1007/s00429-014-0828-3.

43. Kim, Y., Yang, G.R., Pradhan, K., Venkataraju, K.U., Bota, M., García Del Molino, L.C., Fitzgerald, G., Ram, K., He, M., Levine, J.M., et al. (2017). Brain-wide maps reveal stereotyped cell-type-based cortical architecture and subcortical sexual dimorphism. Cell 171, 456–469.e22. https://doi.org/10.1016/j.cell.2017.09.020.

44. Ben Haim, L., and Rowitch, D.H. (2017). Functional diversity of astrocytes in neural circuit regulation. Nat. Rev. Neurosci. 18, 31–41. https://doi.org/10.1038/nrn.2016.159.

45. Marques, S., Zeisel, A., Codeluppi, S., van Bruggen, D., Mendanha Falcão, A., Xiao, L., Li, H., Häring, M., Hochgerner, H., Romanov, R.A., et al. (2016). Oligodendrocyte heterogeneity in the mouse juvenile and adult central nervous system. Science 352, 1326–1329. https://doi.org/10.1126/science.aaf6463.

46. Philips, T., and Rothstein, J.D. (2017). Oligodendroglia: metabolic supporters of neurons. J. Clin. Invest. 127, 3271–3280. https://doi.org/10.1172/JCI90610.

47. Rakic, P. (2009). Evolution of the neocortex: a perspective from developmental biology. Nat. Rev. Neurosci. 10, 724–735. https://doi.org/10.1038/nrn2719.

48. Velmeshev, D., Schirmer, L., Jung, D., Haeussler, M., Perez, Y., Mayer, S., Bhaduri, A., Goyal, N., Rowitch, D.H., and Kriegstein, A.R. (2019). Single-cell genomics identifies cell type-specific molecular changes in autism. Science 364, 685–689. https://doi.org/10.1126/science.aav8130.

49. Lake, B.B., Chen, S., Sos, B.C., Fan, J., Kaeser, G.E., Yung, Y.C., Duong, T.E., Gao, D., Chun, J., Kharchenko, P.V., and Zhang, K. (2018). Integrative single-cell analysis of transcriptional and epigenetic states in the human adult brain. Nat. Biotechnol. 36, 70–80. https://doi.org/10.1038/nbt.4038.

50. Hickey, S.L., Berto, S., and Konopka, G. (2019). Chromatin decondensation by FOXP2 promotes human neuron maturation and expression of neurodevelopmental disease genes. Cell Rep. 27, 1699–1711.e9. https://doi.org/10.1016/j.celrep.2019.04.044.

51. Cadwell, C.R., Palasantza, A., Jiang, X., Berens, P., Deng, Q., Yilmaz, M., Reimer, J., Shen, S., Bethge, M., Tolias, K.F., et al. (2016). Electrophysiological, transcriptomic and morphologic profiling of single neurons using Patch-seq. Nat. Biotechnol. 34, 199–203. https://doi.org/10.1038/nbt.3445.

52. Gouwens, N.W., Sorensen, S.A., Baftizadeh, F., Budzillo, A., Lee, B.R., Jarsky, T., Alfiler, L., Baker, K., Barkan, E., Berry, K., et al. (2020). Integrated morphoelectric and transcriptomic classification of cortical GABAergic cells. Cell 183, 935–953.e19. https://doi.org/10.1016/j.cell.2020.09.057.

53. Jiang, X., Shen, S., Cadwell, C.R., Berens, P., Sinz, F., Ecker, A.S., Patel, S., and Tolias, A.S. (2015). Principles of connectivity among

morphologically defined cell types in adult neocortex. Science *350*, aac9462. https://doi.org/10.1126/science.aac9462.

54. Fuzik, J., Zeisel, A., Máté, Z., Calvigioni, D., Yanagawa, Y., Szabó, G., Linnarsson, S., and Harkany, T. (2016). Integration of electrophysiological recordings with single-cell RNA-seq data identifies neuronal subtypes. Nat. Biotechnol. *34*, 175–183. https://doi.org/10.1038/nbt.3443.

55. Markram, H., Muller, E., Ramaswamy, S., Reimann, M.W., Abdellah, M., Sanchez, C.A., Ailamaki, A., Alonso-Nanclares, L., Antille, N., Arsever, S., et al. (2015). Reconstruction and simulation of neocortical microcircuitry. Cell *163*, 456–492. https://doi.org/10.1016/j.cell.2015.09.029.

56. Masland, R.H. (2004). Neuronal cell types. Curr. Biol. *14*, R497–R500. https://doi.org/10.1016/j.cub.2004.06.035.

57. Zeng, H., and Sanes, J.R. (2017). Neuronal cell-type classification: challenges, opportunities and the path forward. Nat. Rev. Neurosci. *18*, 530–546. https://doi.org/10.1038/nrn.2017.85.

58. Poo, M.M. (2022). Transcriptome, connectome and neuromodulation of the primate brain. Cell *185*, 2636–2639. https://doi.org/10.1016/j.cell.2022.05.011.

59. Scala, F., Kobak, D., Bernabucci, M., Bernaerts, Y., Cadwell, C.R., Castro, J.R., Hartmanis, L., Jiang, X., Laturnus, S., Miranda, E., et al. (2021). Phenotypic variation of transcriptomic cell types in mouse motor cortex. Nature *598*, 144–150. https://doi.org/10.1038/s41586-020-2907-3.

60. Gouwens, N.W., Sorensen, S.A., Berg, J., Lee, C., Jarsky, T., Ting, J., Sunkin, S.M., Feng, D., Anastassiou, C.A., Barkan, E., et al. (2019). Classification of electrophysiological and morphological neuron types in the mouse visual cortex. Nat. Neurosci. *22*, 1182–1195. https://doi.org/10.1038/s41593-019-0417-0.

61. Lee, B.R., Budzillo, A., Hadley, K., Miller, J.A., Jarsky, T., Baker, K., Hill, D., Kim, L., Mann, R., Ng, L., et al. (2021). Scaled, high fidelity electrophysiological, morphological, and transcriptomic cell characterization. eLife *10*, e65482. https://doi.org/10.7554/eLife.65482.

62. González-Burgos, G., Miyamae, T., Krimer, Y., Gulchina, Y., Pafundo, D.E., Krimer, O., Bazmi, H., Arion, D., Enwright, J.F., Fish, K.N., et al. (2019). Distinct properties of Layer 3 pyramidal neurons from prefrontal and parietal areas of the monkey neocortex. J. Neurosci. *39*, 7277–7290. https://doi.org/10.1523/JNEUROSCI.1210-19.2019.

63. Torres-Gomez, S., Blonde, J.D., Mendoza-Halliday, D., Kuebler, E., Everest, M., Wang, X.J., Inoue, W., Poulter, M.O., and Martinez-Trujillo, J. (2020). Changes in the proportion of inhibitory interneuron types from sensory to executive areas of the primate neocortex: implications for the origins of working memory representations. Cereb. Cortex *30*, 4544–4562. https://doi.org/10.1093/cercor/bhaa056.

64. Schwanhäusser, B., Busse, D., Li, N., Dittmar, G., Schuchhardt, J., Wolf, J., Chen, W., and Selbach, M. (2011). Global quantification of mammalian gene expression control. Nature *473*, 337–342. https://doi.org/10.1038/nature10098.

65. Liu, Y., Beyer, A., and Aebersold, R. (2016). On the dependency of cellular protein levels on mRNA abundance. Cell *165*, 535–550. https://doi.org/10.1016/j.cell.2016.03.014.

66. Greenbaum, D., Colangelo, C., Williams, K., and Gerstein, M. (2003). Comparing protein abundance and mRNA expression levels on a genomic scale. Genome Biol. *4*, 117. https://doi.org/10.1186/gb-2003-4-9-117.

67. Kwon, S., Chin, K., Nederlof, M., and Gray, J.W. (2017). Quantitative, in situ analysis of mRNAs and proteins with subcellular resolution. Sci. Rep. *7*, 16459. https://doi.org/10.1038/s41598-017-16492-1.

68. Chaudhuri, R., Knoblauch, K., Gariel, M.A., Kennedy, H., and Wang, X.J. (2015). A large-scale circuit mechanism for hierarchical dynamical processing in the primate cortex. Neuron *88*, 419–431. https://doi.org/10.1016/j.neuron.2015.09.008.

69. Passingham, R.E., and Wise, S.P. (2012). The Neurobiology of the Prefrontal Cortex: Anatomy, Evolution, and the Origin of Insight (Oxford University Press).

70. Gămănuţ, R., Kennedy, H., Toroczkai, Z., Ercsey-Ravasz, M., Van Essen, D.C., Knoblauch, K., and Burkhalter, A. (2018). The mouse cortical connectome, characterized by an ultra-dense cortical graph, maintains specificity by distinct connectivity profiles. Neuron *97*, 698–715.e10. e610. https://doi.org/10.1016/j.neuron.2017.12.037.

71. Park, J.E., and Silva, A.C. (2019). Generation of genetically engineered non-human primate models of brain function and neurological disorders. Am. J. Primatol. *81*, e22931. https://doi.org/10.1002/ajp.22931.

72. Jennings, C.G., Landman, R., Zhou, Y., Sharma, J., Hyman, J., Movshon, J.A., Qiu, Z., Roberts, A.C., Roe, A.W., Wang, X., et al. (2016). Opportunities and challenges in modeling human brain disorders in transgenic primates. Nat. Neurosci. *19*, 1123–1130. https://doi.org/10.1038/nn.4362.

73. Bakken, T.E., Hodge, R.D., Miller, J.A., Yao, Z., Nguyen, T.N., Aevermann, B., Barkan, E., Bertagnolli, D., Casper, T., Dee, N., et al. (2018). Single-nucleus and single-cell transcriptomes compared in matched cortical cell types. PLoS One *13*, e0209648. https://doi.org/10.1371/journal.pone.0209648.

74. Dobin, A., Davis, C.A., Schlesinger, F., Drenkow, J., Zaleski, C., Jha, S., Batut, P., Chaisson, M., and Gingeras, T.R. (2013). STAR: ultrafast universal RNA-seq aligner. Bioinformatics *29*, 15–21.

75. Zeisel, A., Hochgerner, H., Lönnerberg, P., Johnsson, A., Memic, F., van der Zwan, J., Häring, M., Braun, E., Borm, L.E., La Manno, G., et al. (2018). Molecular architecture of the mouse nervous system. Cell *174*, 999–1014.e22. https://doi.org/10.1016/j.cell.2018.06.021.

76. Ximerakis, M., Lipnick, S.L., Innes, B.T., Simmons, S.K., Adiconis, X., Dionne, D., Mayweather, B.A., Nguyen, L., Niziolek, Z., Ozek, C., et al. (2019). Single-cell transcriptomic profiling of the aging mouse brain. Nat. Neurosci. *22*, 1696–1708. https://doi.org/10.1038/s41593-019-0491-3.

77. Yuste, R., Hawrylycz, M., Aalling, N., Aguilar-Valles, A., Arendt, D., Armañanzas, R., Ascoli, G.A., Bielza, C., Bokharaie, V., Bergmann, T.B., et al. (2020). A community-based transcriptomics classification and nomenclature of neocortical cell types. Nat. Neurosci. *23*, 1456–1468. https://doi.org/10.1038/s41593-020-0685-8.

78. He, K., Gkioxari, G., Dollar, P., and Girshick, R. (2020). Mask R-CNN. IEEE Trans. Pattern Anal. Mach. Intell. *42*, 386–397. https://doi.org/10.1109/TPAMI.2018.2844175.

79. Saleem, K.S., and Logothetis, N. (2007). A Combined MRI and Histology Atlas of the Rhesus Monkey Brain in Stereotaxic Coordinates (Academic).

80. Crow, M., Paul, A., Ballouz, S., Huang, Z.J., and Gillis, J. (2018). Characterizing the replicability of cell types defined by single cell RNA-sequencing data using MetaNeighbor. Nat. Commun. *9*, 884. https://doi.org/10.1038/s41467-018-03282-0.

81. Marcus, D., Harwell, J., Olsen, T., Hodge, M., Glasser, M., Prior, F., Jenkinson, M., Laumann, T., Curtiss, S., and Van Essen, D. (2011). Informatics and data mining tools and strategies for the human connectome project. Front. Neuroinformat *5*, 4.

STAR★METHODS

KEY RESOURCES TABLE

REAGENT or RESOURCE	SOURCE	IDENTIFIER
Antibodies		
Anti-NeuN Antibody	Sigma-Aldrich	RRID: AB_2298772
Goat Anti-Mouse IgG	Vector Lab	RRID: AB_2336171
Biological samples		
#1 Cynomolgus monkeys (6-year-old, 4.2 kg)	This study	N/A
#2 Cynomolgus monkeys (4-year-old, 3.7 kg)	This study	N/A
#3 Cynomolgus monkeys (7-year-old, 10.6 kg)	This study	N/A
Chemicals, peptides, and recombinant proteins		
Normal Goat Serum Blocking Solution	Vector Lab	S-1000-20
VECTASTAIN® ABC-HRP Kit	Vector Lab	PK-4000
RNAscope® Wash Buffer Reagents	Advanced Cell Diagnostic	Cat.No.310091
RNAscope® Target Retrieval Reagents	Advanced Cell Diagnostic	Cat.No.322000
RNAscope® H2O2 and Protease Reagents	Advanced Cell Diagnostic	Cat.No.322381
RNAscope® Multiplex Fluorescent Detection Reagents v2	Advanced Cell Diagnostic	Cat.No.323110
RNAscope® Multiplex TSA Buffer	Advanced Cell Diagnostic	Cat.No.322810
550/570 nmm Opal 570 Reagent Pack	Akoya	FP1488001KT
TSA Vivid Fluorophore 650	Advanced Cell Diagnostic	Cat.No.323273
DAPI Fluromount-G®	SouthernBiotech	Cat.No.0100-20
Probe Diluent	Advanced Cell Diagnostic	Cat.No.300041
20 × PBS Buffer	Sangon Biotech	B548117-0500
Paraformaldehyde	Sigma-Aldrich	P6148-1KG
Tissue-Tek OCT	Sakura	4583
AMPure XP Beads	Vazyme	N411-03
ssDNA reagent	Invitroge	Q10212
20 × SSC	Ambion	AM9770
Pepsin	Sigma	P7000
RNase inhibitor	NEB	M0314L
Exonuclease I	NEB	M0293L
Qubit™ dsDNA Assay Kit	INVITROGEN	Q32854
EDTA	INVITROGEN	15575-038
ConA Rhodamine	Vector	RL-1002
Deposited data		
Public Single-nucleus RNA sequencing data of human PFC	NCBI SRA	SRA: PRJNA434002
Public Single-nucleus RNA sequencing data of human F1	NeMO Archive	nemo: dat-ek5dbmu
Public Single-nucleus RNA sequencing data of human V1	GEO	GEO: GSE97942
Public Single-cell RNA sequencing data of mouse PL-ILA-ORB	NeMO Archive	nemo: dat-jb2f34y
Public Single-nucleus RNA sequencing data of mouse F1	NeMO Archive	nemo: dat-ek5dbmu

Continued

REAGENT or RESOURCE	SOURCE	IDENTIFIER
Public Single-cell RNA sequencing data of mouse V1	NeMO Archive	nemo: dat-jb2f34y
Public Single-nucleus RNA sequencing data of human 32, 25, 13 regions	NeMO Archive	RRID:SCR_016152
Raw data of stereo-seq and snRNA-seq data	This study	https://db.cngb.org/search/project/CNP0002035
Processed data of stereo-seq and snRNA-seq data	This study	https://macaque.digital-brain.cn/spatial-omics
Oligonucleotides		
RNAscope® Probe- Mfa-TSHZ2-C1	Advanced Cell Diagnostic	1229081-C1
RNAscope® Probe- Mfa-EPHA3-C2	Advanced Cell Diagnostic	1229011-C2
RNAscope® Probe-Mfa-FOXP2-C3	Advanced Cell Diagnostic	1229021-C3
RNAscope Probe - Mmu-SST	Advanced Cell Diagnostic	461681
Stereo-seq-TSO: CTGCTGACGTACTGAGAGGC/rG//rG//iXNA_G/	Sangon	N/A
cDNA PCR primer: CTGCTGACGTACTGAGAGGC	Sangon	N/A
Stereo-seq-library-F: /5phos/CTGCTGACGTACTGAGAGG*C*A	Sangon	N/A
Stereo-seq-library-R: GAGACGTTCTCGACTCAGCAGA	Sangon	N/A
Stereo-seq-library-splint-oligo: GTACGTCAGCAGGAGACGTTCTCG	Sangon	N/A
Stereo-seq-read1: CTGCTGACGTACTGAGAGGCATGGCGACCTTATCAG	Sangon	N/A
Stereo-seq-MDA-primer: TCTGCTGAGTCGAGAACGTC	Sangon	N/A
Stereo-seq-read2: GCCATGTCGTTCTGTGAGCCAAGGAGTT	Sangon	N/A
Software and algorithms		
R	https://cran.r-project.org/	V4.0.3
Seurat	https://satijalab.org/seurat/	V4.1.1
SeuratDisk	https://github.com/mojaveazure/seurat-disk	V0.0.0.9020
Spatial-ID	https://github.com/TencentAILabHealthcare/spatialID	Nov 17, 2022
MetaNeighbor	https://github.com/gillislab/MetaNeighbor-BICCN	V1.10.0
clusterProfiler	http://www.bioconductor.org/packages/release/bioc/html/clusterProfiler.html	V3.18.1
Monocle2	https://github.com/Scylardor/Monocle2	V2.20.0
pheatmap	http://mirrors.ustc.edu.cn/CRAN/web/packages/pheatmap/index.html	V1.0.12
ggplot2	https://cran.rstudio.com/web/packages/ggplot2/index.html	V3.3.6
ggtree	https://github.com/YuLab-SMU/ggtree	V3.0.4
ggfx	GitHub - thomasp85/ggfx: Filters and Shaders for 'ggplot2'	V1.0.1
ggnet	GitHub - briatte/ggnet: Network visualization with ggplot2	V0.1.0
ggpubr	GitHub - kassambara/ggpubr: 'ggplot2' Based Publication Ready Plots	V0.5.0

(Continued on next page)

Continued

REAGENT or RESOURCE	SOURCE	IDENTIFIER
org.Hs.eg.db	https://bioconductor.org/packages/release/data/annotation/html/org.Hs.eg.db.html	V3.14.0
enrichplot	https://bioconductor.org/packages/release/bioc/html/enrichplot.html	V1.14.2
eulerr	https://cran.r-project.org/web/packages/eulerr/vignettes/introduction.html	V6.1.1
tidyverse	https://www.tidyverse.org/	V1.3.2
ComplexHeatmap	GitHub - jokergoo/ComplexHeatmap: Make Complex Heatmaps	V2.10.0
python	https://www.python.org/	V3.8.13
scanpy	https://pypi.org/project/scanpy/	V1.9.1
numpy	https://pypi.org/project/numpy/	V1.22.3
pandas	https://pypi.org/project/pandas/	V1.4.3
bbknn	https://github.com/Teichlab/bbknn	V1.5.1
Metascape	https://metascape.org/	N/A
ANTs	https://github.com/ANTsX/ANTs	V2.3.5
HCP workbench	https://humanconnectome.org/software/connectome-workbench	V1.5.0
Matlab	https://www.mathworks.com/products/new_products/release2019b.html	R2019b
scrattch.hicat	https://github.com/AllenInstitute/scrattch.hicat	v1.0.0

RESOURCE AVAILABILITY

Lead contact
Further information and requests for the resources and reagents may be directed to and will be fulfilled by the lead contact, Chengyu Li (tonylicy@ion.ac.cn).

Materials availability
All materials used for stereo-seq and snRNA-seq are commercially available.

Data and code availability
- The processed data ready for exploration can be accessed and downloaded via https://macaque.digital-brain.cn/spatial-omics. All raw data have been deposited to CNGB Nucleotide Sequence Archive (accession code: CNP0002035, https://db.cngb.org/search/project/CNP0002035) and are publicly available as of the date of publication. Accession numbers are listed in the key resources table.
- All data were analyzed with standard programs and packages, as detailed in the key resources table. Custom code of AI-assisted single cell segmentation algorithm is available at https://github.com/TencentAILabHealthcare/Cell_Segmentation_Fluorescence.
- Additional information required to reanalyze the data reported in this paper is available from the lead contact upon request.

EXPERIMENTAL MODEL AND STUDY PARTICIPANT DETAILS

Animal care
Animal protocol was approved (ION-2019011) by the Biomedical Research Ethics Committee of CAS Center for Excellence in Brain Science and Intelligence Technology, Chinese Academy of Sciences. Animal care complied with the guideline of this committee. Left hemispheres were collected from three male cynomolgus monkeys (*M. fascicularis*; #1, 6-year-old, 4.2 kg; #2, 4-year-old, 3.7 kg; #3, 7-year-old, 10.6 kg).

METHOD DETAILS

Tissue collection

The animals were deeply anesthetized with tiletamine hydrochloride, zolazepam hydrochloride (25 mg/kg, I.M) and xylazine hydrochloride (20 mg/kg, I.M). The brain was quickly perfused at room temperature with artificial cerebrospinal fluid (ACSF, 0.6 L/kg, and perfusion speed 100 mL/min through the heart) bubbled with oxygen (influx with a mixture of 95% O_2 and 5% CO_2), followed with prechilled bubbled ACSF (4°C, 100mL/min). Using a stereotaxic device and a micromanipulator (SMM-200, Narishige), we coronally cut through central sulcus and divided the left hemisphere into anterior and posterior blocks. The isolated brain blocks were quickly wiped dry with sterile gauze and mixed thoroughly with 4°C OCT (4583#, Sakura). Subsequently the brain blocks were transferred to a metal mold fully embedded with 4°C OCT, quickly frozen on dry ice, and then stored in -80°C refrigerator. To minimize RNA degradation, all solutions were prepared with sterilized water containing diethyl pyrocarbonate (DEPC) (B501005-0005, Sangon Biotech), and all instruments were washed with sterilized water containing DEPC and RNase Zap (AM9780, Invitrogen). The whole tissue collection process was completed within 30 min.

Tissue cryosection and section flattening

Before cryosection, temperature of the cooling chamber was set to -20°C. The tools involved (chip, forceps, brush and blade) were placed in the cryostat chamber in advance for pre-cooling. Immediately before sectioning, anterior and posterior blocks were placed into two separate cryostats (Thermo Fisher Cryostar NX50). At each desired coronal coordinate, cryosection was performed to obtain one 10-μm section for Stereo-seq, two 10-μm sections for immunohistochemical staining, and three-five 50-μm sections for snRNA-seq. Block face images were taken for each coordinate. Between successive days of sectioning, the tissue blocks were stored at -80°C. The thin Stereo-seq sections were firstly flattened on cold metal plane (-20°C) in cryostat by soft brush and plastic tweezers. Then the section was carefully placed onto the precooled Stereo-seq chip (-20°C). To attach a tissue section progressively on the entire chip, a Stereo-seq section was placed manually on operator's hand to gradually raise section temperature on Stereo-seq chip. This procedure enables tissue attachment without air bubbles and tissue folding.

Tissue-section processing for stereo-seq

The tissue section on the Stereo-seq chip (5 cm x 3 cm or 2 cm x 3 cm) was then incubated at 37°C for 5-8 min and subsequently fixed in methanol (Sigma, 34860, precooled for 30 mins at -20°C; 40 ml methanol was added in 10 cm dish for each section) and incubated at -20°C for 30 minutes. Methanol was then dried out in a hood. Tissue section on the chip was then stained with mixture of nucleic acid reagent (Invitrogen, Q10212) and conA Rhodamine (Vector, RL-1002, working concentration 200 μg/ml) for 5 min and subsequently washed with 0.1x SSC buffer (Ambion, AM9770; containing 0.05 U/μl RNase inhibitor). Section images were captured using Zeiss Axio Scan Z1 microscope (at EGFP wavelength, 10-ms exposure). Tissue sections were then permeated by incubating in 0.1% pepsin (Sigma, P7000) at 37°C for 15 minutes (pepsin was prewarmed at 37°C for 3 min) in 0.01M HCl buffer (pH 2) and then washed with 0.1xSSC buffer (containing 0.05 U/μl RNase inhibitor) to remove pepsin. In this step, RNAs were released from the permeated tissue and captured by Stereo-seq chip. RNAs were then reverse transcribed for 2 hours at 42°C. After reverse transcription, tissue sections were washed with 0.1x SSC buffer and digested with tissue removal buffer (10 mM Tris-HCl, 25 mM EDTA, 100 mM NaCl, 0.5% SDS) at 55°C for 30 min, and then the chips were washed twice with 0.1x SSC buffer. The cDNA-containing chips were then subjected to Exonuclease I (NEB, M0293L) treatment for 1 hour at 37°C and were washed once with 0.1x SSC buffer. The cDNAs were amplified with Hot Start DNA Polymerase (QIAGEN). The PCR reaction protocol was: first incubation at 95°C for 5 min, 15 cycles at 98°C for 20 s, 58°C for 20 s, 72°C for 3 min and a final incubation at 72°C for 5 min. The PCR products were then purified using 0.6 x VAHTSTM DNA Clean Beads and were quantified by Qubit dsDNA HS assay kit (Invitrogen, Q32854).

Library preparation and sequencing

One-hundred ng of cDNA (20 μl) from each sample were tagmented with Tn5 transposases (Vazyme) at 55°C for 10 mins, then the reaction was stopped by adding 5 μL of 0.02% SDS. PCR reaction mix (75 μL, Library HIFI Master Mix, Library PCR primer mix) was added to each fragmented cDNA sample. Samples were then transferred to a thermal cycler for amplification using the following protocol: 1 cycle at 95°C for 5 min, 13 cycles of tri-temperature reaction (98°C 20 s, 58°C 20 s and 72°C 30 s), and 1 cycle at 72°C for 5 min. After amplification, the PCR products were purified with 0.6x and 0.2x VAHTSTM DNA Clean Beads (VAZYME, N411-03) and were used for DNB (DNA Nano Ball) generation. Finally, the DNBs were sequenced on the DNBSEQ™ T10 sequencing platform (MGI, Shenzhen, China) with 50 bp read1 and 100 bp read2.

Immunohistochemical staining

Coronal sections adjacent to Stereo-seq chips were collected for IHC staining with NeuN antibody, which recognizes the DNA-binding, neuron-specific protein NeuN. The 10-μm sections were mounted on gelatinized glass slides, and baked to dry for 5 min at 37 °C. The mounted brain tissues were fixed with 4% paraformaldehyde in 0.1M phosphate buffer (PBS) for 10 min. After three washes in PBS, the sections were pre-incubated for 15 min in 0.5% Triton X-100 in PBS, and then 1 hour in blocking solution containing 10% normal goat serum and 0.1% Triton X-100 in PBS (0.1% PBST). Then the sections were incubated overnight at 4°C in 0.1% PBST containing the monoclonal antibody NeuN (Sigma-Aldrich, 1:1500). After three washes in PBS, the sections were incubated for

30 min in 0.1% PBST containing 0.6% hydrogen peroxide to block endogenous peroxidase that might contribute to background staining. After three washes in PBS, the sections were incubated in PBS containing biotinylated secondary antibody (1:200) for 2 hours, washed three times in PBS, and transferred to PBS containing the peroxidase conjugate from the Vectastain CBC kit (Vector Laboratories, Burlingame, CA). After rinsing three times in PBS, the sections were immersed in a solution of 0.05% 3-3'diaminoben-zidine-4HCl (DAB, Sigma-Aldrich, St Louis, MO) and 0.05% hydrogen peroxide. After staining, the sections were dehydrated in increasing concentrations of ethanol, cleared in xylene and coverslipped with DPX medium. Subsequently, the glass-mounted sections were scanned at 5× (0.88 μm/pixel) in a Zeiss scanner to generate images.

RNA in situ hybridization (RNAscope)
The RNAscope procedures were conducted in accordance with the manufacturer's instructions using the RNAscope® Multiplex Fluorescent Reagent Kit v2 (Cat. No. 323100). Fixed frozen tissues from an 18-year-old female cynomolgus monkey (M. fascicularis) were used to prepare 14-μm thick sections, which were mounted on SuperFrost Plus Slides (Fisher Scientific, Cat. No. 12-550-15). The sections were air-dried for 2 hours at -20°C and then stored with desiccants at -80°C. Prior to hybridization, the slides were washed with PBS for 5 minutes and baked for 30 minutes at 60°C. The sections were post-fixed with pre-chilled 4% paraformalde-hyde in PBS for 15 minutes at 4°C, followed by dehydration with gradient alcohol. The RNAscope® Hydrogen Peroxide was added to cover the entire section, and the slides were incubated for 10 minutes at room temperature. The slides were then washed in distilled water. To prepare the sections for hybridization, they were boiled for 5 minutes in the RNAscope 1X Target Retrieval Reagent and incubated for 30 minutes in RNAscope Protease III at 40°C. The sections were then hybridized with each probe (FOXP2, EPHA3, SST) in a HybEZ oven (Advanced Cell Diagnostics, Newark, CA, USA) for 2 hours at 40°C. The RNAscope Multiplex Fluorescent Re-agent Kit v2 was used to visualize the signal, and section images were captured using a Zeiss Axio Scan Z1 microscope (10×, 0.65 μm/pixel).

Brain tissue collection for snRNA-seq
For monkey #1, the snRNA-seq samples were collected from frozen sections adjacent to those for Stereo-seq. These sections were cut at 50-μm thickness, and 3 to 5 sections for each coronal coordinate were collected for snRNA-seq analysis. Sections were transferred into plastic wells on dry ice and stored in a -80 °C refrigerator. Each section was further segmented into distinct areas on dry ice using tissue punchers (5 - 8 mm in diameter). Tissues at the same brain regions (e.g., around the same sulcus) were combined in a prechilled pipe as one sample. For monkey #2, the snRNA-seq samples were dissected from block-face cortical regions of the hemi-sphere contralateral to that used for Stereo-seq. In the cryostat, the cortical areas were segmented at 1 – 2 mm depth using tissue punchers (2.5 - 4 mm in diameter). After dissection, the samples were immediately frozen in liquid nitrogen and then kept in dry ice or -80 °C refrigerator. Throughout the sampling manipulation, the tissues were carefully transferred to pre-cold tube without thawing.

Single-nucleus suspension preparation
Single nucleus suspension was prepared as previously described.[73] Briefly, frozen monkey brain tissue pieces were placed in Dounce homogenizer with 2 ml pre-chilled homogenization buffer and kept the Dounce homogenizer on ice during grinding. Tissue was homogenized with 10-15 strokes of the pestle A and followed by 10-15 strokes of the pestle B, then added 2 ml homogenization buffer to the Dounce homogenizer and filtered the homogenate through 30 μm MACS SmartStrainers (Miltenyi Biotech, #130-110-915) into 15 ml conical tube and centrifuged at 500 g for 5 mins at 4°C to pellet nuclei, then the pellet was resuspended in 1.5 ml of blocking buffer and centrifuged at 500 g for 5 mins at 4°C to pellet nuclei. Nuclei were resuspended with cell resuspension buffer for subsequent snRNA-seq library preparation.

snRNA-seq library construction and sequencing
The DNBelab C Series High-throughput Single-Cell RNA Library Preparation Kit (MGI, #940-000047-00) was utilized to construct the sequencing libraries according to the manufacturer's protocol. In brief, single-nucleus suspensions were used for droplet generation, emulsion breakage, beads collection, reverse transcription, second-strand synthesis, cDNA amplification and droplet index product amplification to generate barcoded libraries. The sequencing libraries were quantified by Qubit™ ssDNA Assay Kit (Thermo Fisher Scientific, #Q10212) and sequenced on the ultra-high-throughput DIPSEQ T1 or DIPSEQ T10 sequencers sequencer at the China National GeneBank (Shenzhen, China).

snRNA-seq data processing
The sequencing data were processed as previously described.[29] First, bead barcodes and unique molecular identifier (UMI) se-quences were extracted using parse function in PISA (https://github.com/shiquan/PISA). For cDNA libraries, 1-10bp and 11-20bp of read1 were bead barcodes, the 21-30bp was UMI sequence, the whole read2 (100bp) was used for downstream alignment anal-ysis. For the Droplet Index libraries, 1-10bp and 11-20bp of read1 sequences were bead barcodes, the 1-10bp of read2 was UMI sequence, the 11-20bp and 21-30bp of read2 were droplet index barcodes. Reads with improper barcodes according to the barcode list were excluded. To map the pre-mRNA fragments which may cover both exonic and intronic regions, we created a modified GTF annotation file from ensemble release-91 which only contain transcript regions, and the original annotation rows for exons were all deleted, then we replaced the feature type name from 'transcript' to 'exon'. Then the snRNA-seq data were aligned to *Macaca*

fascicularis genome (5.0.91) reference using STAR (v2.5.3)[74] with the modified GTF file described above. To estimate the actual number of beads, we used the "barcodeRanks" function of DropletUtils tool to find the threshold value of sharp transition in total UMI counts distribution. Beads with UMI counts less than the threshold were removed. We merged the beads considered to be one cell,[29] and counted the gene expression of cells by PISA.

We next filtered out libraries for quality control using the following criteria: 1) Reads with proper barcodes less than 1,000,000, 2) overall mapping ratio less than 85%, and 3) estimated number of cells less than 1,000 (except for 6 cerebellum libraries). As a result, 444 snRNA-seq libraries covering different brain areas among two macaques were included for further downstream analysis.

Cell clustering and cell-type identification using snRNA-seq data

Basic processing and visualization of the snRNA-seq data were performed with the Scanpy (v.1.9.1) in Python (v.3.8.13). We discarded cells with the number of genes (nFeatureRNA) less than 1000, the molecule to gene ratio (nCount/nFeature) less than 1.2 and the percentage of mitochondrial genes (percent.mt) larger than 5%. After the first quality control, 1,493,240 cells were remained for the following analyses. The data were log normalized and scaled to 10,000 transcripts per cell. Genes with high variations across cells were identified with the "sc.pp.highly_variable_genes" function with default parameters (top 3000). Next, principal component analysis (PCA) was carried out, and the top 40 principal components (PCs) were used by BBKNN method to remove the batch effect among two macaques. Graph-based clustering (Leiden) was performed with resolution of 1.0 on the graph-representation output of BBKNN. This method resulted in 33 cell clusters. We used uniform manifold approximation and projection (UMAP) method to visualize the distance between cells in 2D space. We then categorized the 33 cell clusters into 3 categories based on classical marker genes, including glutamatergic neurons, GABAergic neurons and non-neuronal cells. Then the three categories of cells were further iteratively classified into more cell clusters with higher resolution. A total of 264 cell clusters were kept after removing clusters with low quality, with the number of cells less than 100, or doublets (expressing marker genes of multiple cell types). We applied wilcoxon rank sum test using the "sc.tl.rangk_genes_groups" function for differential gene expression analysis among clusters. Genes with $\log_2$ fold-change > 1 and FDR < 0.05 were retained as significant marker genes for the cluster. We compared the top 50 ranked marker genes of each pair of cell clusters by calculating Jaccard similarity, and combined clusters with Jaccard similarity larger than 0.8. We also removed outlier cells for each cluster based on the distance to the center point. A random forest classifier was used to assess the robustness of the various cell clusters. The top 50 DEG were selected as features, and 100 cells were randomly sampled from each cluster, of which 80% of the cells were used to train the model, and the rest 20% as a validation dataset. This procedure was done with "tuneRF", "randomForest", and "predict" functions of randomForest R package (v.4.7.1.1). For each cell type, we used previously reported marker genes to determine the subclass label of each cell-type.[75–77] To build a dendrogram of cell types, we used a correlation matrix based on median expression values for the top 50 most significant marker genes of each cluster with function "build_dend" from the scrattch.hicat package.

Prediction of the projection properties of glutamatergic cell subclasses

Transcriptome profiles of glutamatergic neurons from our data and published data were integrated by the "IntegrateData" function of Seurat R package (v 4.3.0) with the marker genes as anchors. Then principal component analysis (PCA) was carried out and the top 86 components were used for downstream analysis. The integrated datasets were re-clustered with k.param = 20 and resolution = 0.5 using "FindNeighbors" and "FindClusters" functions. Finally, the projection property of each glutamatergic cell subclass was inferred by the previously projection-property-defined cell type with the most frequent co-embedding in the integrated clustering. The correspondence between glutamatergic cell subclasses and previous defined cell types were shown by the "sankeyNetwork" function of networkD3 R package (v 0.4).

Stereo-seq data processing

The fastq files of Stereo-seq were processed according to the previously described workflow.[28] The first reads of the Stereo-seq data contained CID (coordinate Identity) sequences, which were aligned to the designed coordinates of the Stereo-seq chip obtained from the first round of sequencing. A maximum of 1 base mismatch was allowed during the alignment process. Reads with MID (molecular Identifiers) containing N bases or more than 2 bases with quality score lower than 10 were removed from the dataset. The CID and MID associated with each read were added to the read header. The retained reads were then aligned to the reference genome using STAR[74] and reads with mapping quality score > 10 were counted and annotated to their corresponding genes. UMIs that have the same CID (coordinate Identity) and gene locus were combined into a single UMI, allowing for 1 mismatch to correct for sequencing and PCR errors. Finally, this information was used to generate a CID-containing expression profile matrix. The entire pipeline SAW can be accessed at https://github.com/STOmics/SAW.

Image-based single-cell segmentation of stereo-seq data

For single cell segmentation of the Stereo-seq data, nucleic acid staining images were automatically registered into mRNA coordinate space based on periodical track lines pre-engraved in the chip plane. In this step, the captured mRNAs of a section were treated as an image with the UMI counts at each position as its pixel value. On both nucleic acid staining and mRNA images, we applied 1D Laplacian of Gaussian (LoG) operators (sigma = 5e-4) along the row and column directions respectively to detect track lines, following two rules: (1) The track lines are most likely located at where the intensity values change rapidly in the images, which can be identified

at the peaks through a LoG filter. (2) The registered track lines should roughly lie along the horizontal or vertical directions. We then obtained the averaged angle between the detected track lines in the nucleic acid staining image and those in the corresponding RNA image as the rotation angle between the two images. Next, we used the averaged interval of the periodical track lines in both nucleic acid staining and mRNA images to compute the relative scale. Finally, we calculated the relative translation using RANSAC algorithm (min_samples = 3, residual_threshold = 5) with the detected track lines in the mRNA images and the rotated and scaled track lines in the nucleic acid staining images as inputs. With the rotation, scale and translation parameters, nucleic acid staining images can be registered into the coordinate space of mRNA images. The whole registration was implemented with Scikit-image package (v.0.18.3) in Python (v.3.9.7).

Cells in nucleic acid staining images were automatically segmented through a deep learning model trained using annotations by ConA staining image. ConA staining images stain the membranes of cells, forming clear boundaries between cells, where cells are easier to be distinguished and manually marked than using nucleic acid staining images alone. However, ConA images have the problem of under-staining where not all cells would be clearly stained, and it is also tedious to manually mark every cell on the image. Therefore, we designed an active learning procedure. We first manually marked cells which could be clearly identified in ConA staining images. Starting with this small set (hundreds of cells), we trained a deep learning model (i.e. mask R-CNN[78]) on the ConA staining images, called ConA model. We utilized a total of 7 ConA images to construct the ConA model. One of these images was manually labeled and kept aside for validation purposes. The remaining 6 ConA images were employed for model training and underwent manual correction. The training process was conducted progressively as follows: Initially, we manually labeled the first image to train the initial ConA model. Subsequently, this trained ConA model was used to predict cell labels on the second unlabeled ConA image. After manual correction, the newly labeled ConA image was included in the training set to update the ConA model. This process was repeated until all 7 ConA images had their labels corrected. Subsequently, these corrected labels were transferred to their corresponding nucleic acid images for training the nucleic acid model. The ConA model was specifically utilized to aid in the generation of cell labels. After several iterations, a full set of cell annotations on ConA staining images were generated (14212 in the current experiment). The detailed information of the active learning procedure can be found in Table S4. After that, the cell annotations were transferred to the corresponding nucleic acid staining images to train another deep learning model on the nucleic acid staining images, called nucleic acid model. Noted that the nucleic acid model was trained with incomplete annotations since ConA images have fewer stained cells than nucleic acid images. Therefore, a low score threshold of 0.1 was applied to retain more cells. The nucleic acid model was deployed on nucleic acid staining images to obtain single cell segmentation. The nucleic acid model was validated on 10,209 cells from three nucleic acid staining images and achieved 0.912 of precision and 0.913 of recall, demonstrating reliable performance. All models described in this step were implemented with mmdet package (v.2.25.1) in Python (v.3.8.13).

Cortical region and layer parcellation

According to atlas-based landmarks,[79] the macaque cortex were segmented into 143 brain regions, including prefrontal, frontal, cingulate, somatosensory, insular, auditory, temporal, parietal, occipital and piriform areas. For each coronal section, the cortical region and layer parcellation were manually delineated on Stereo-seq data background, based on cytoarchitectual pattern (eg. cell density, cell size) revealed by total mRNA expression, nucleic acid staining, and NeuN staing of adjacent sections.

Stereo-seq data preprocessing

The signal of each gene in all pixels that fell within the segmentation boundaries of the cells was summarized and merged with the location information matrix. The sequencing data within the manually annotated cortex region were processed with the Seurat package in R. The cell-by-gene matrix was obtained with the function "CreateSeuratObject" with min.cells = 3 and min.features = 0. The percentage of mitochondrial genes (percent.mt) was calculated with the function "PercentageFeatureSet" (using genes *ND6, COX3, COX1, ND5, ND4, ND2, ND4L, ATP8, CYTB, COX2, ND3, ATP6* and *ND1*). Cells with less than 100 features or percent.mt larger than 15% were discarded. In order to mitigate potential batch effects resulting from variations in single-cell sequencing depth within and across sections of the Stereo-seq map, "SCTransform" with the parameter vars.to.regress = "percent.mt" was used for normalization.

Cell-type annotation of single cells in the stereo-seq map

To annotate single cells on Stereo-seq data with cell types classified by snRNA-seq analysis, we employed a recently developed cell type annotation algorithm, spatial-ID.[31] First, a four-layer deep neural network (DNN) with two hidden layers of 2048 and 1024 nodes was trained with snRNA-seq data (learning rate = 3e-4, weight decay = 1e-6). The trained DNN was used to compute the initial probabilities of defined cell types for each single cell on the Stereo-seq data. Then the spatial neighborhood information of cells on Stereo-seq data was encapsulated into an adjacency matrix with normalized Euclidean distances as values for non-zero elements. Next, a graph convolution network (GCN) took the initial probabilities, the distance-weighted adjacency matrix and the original gene expression of cells as inputs to generate the final probabilities of cell types for each cell. The GCN contained two autoencoders, that is, a deep autoencoder for gene expression representations and a variational graph autoencoder for spatial neighborhood information representations, and a classifier block. The two autoencoders were trained by reconstruction losses via a self-supervised learning strategy, forcing the model to focus on the features of Stereo-seq data itself. The classifier block was trained by a Cross Entropy loss to refine the cell type probabilities epoch by epoch. The number of training epoch of the GCN was set to 200. The weights

for the reconstruction loss and the classification loss were set to 1 and 50, respectively. Finally, the cell type with the maximal probability produced by the GCN was assigned as the annotation for each single cell. Spatial-ID used in this study was implemented with PyTorch package (v.1.13.1) and PyTorch Geometric package (v.2.1.0) in Python (v.3.8.10). By utilizing the cell-type registration method (Spatial-ID) to annotate single cells for each Stereo-seq section, the influence of batch effects (across different sections) in clustering and cell type annotation was circumvented. The high consistency in cell type distributions between adjacent sections or sections with similar coordinates from different biological replicates confirmed the reliability of this procedure (Figures S2F–S2H).

Quantification of spatial distribution of various cell types in the stereo-seq map

We quantified the number of cells annotated with specific cell types in each monkey and cell types with more than 1000 cells in the three monkeys were used for the following analysis. For each cell type, we quantified the density in each layer and cortical region by dividing the total number of cells in each area by the area size. To quantify the layer distribution of various glutamatergic neuron types, we performed z-score transformation of cell density in each cortical layer for each cell type, and layers with z-score larger than 0 were used to annotate the subclass name of each glutamatergic cell type together with marker gene expression.

Correspondence of cell types between stereo-seq and snRNA-seq data

The snRNA-seq data was normalized with the R package Seurat. The data slot of SCT assay was reformatted and used as input with the function SingleCellExperiment. The top variable genes included in the slot scale.data were used for the parameter var_genes in the function trainModel of the package MetaNeighbor.[80] As for Stereo-seq data, normalization was conducted as mentioned above. The function MetaNeighborUS was utilized with the parameter one_vs_best = TRUE for the data slot of SCT assay of the stereo-seq data.

Neighborhood complexity

Qualified regions were manually selected for neighborhood complexity analysis. Cell-cell distance matrices were calculated with the function "dist" in R. The neighborhood complexity of a cell is defined as the number of different cell clusters present within a neighborhood of 200 pixel, or 100 μm, in radius surrounding the given cell. Downstream analysis was conducted with the Seurat package. Based on the cell-by-neighbor-cluster-cell-number matrix, we used the function "NormalizeData" and "ScaleData" with default parameters for preprocess and then the function "RunPCA" and "RunUMAP" with the parameter npcs = 20 and dims = 1:20 for dimension reduction.

Region-specific cell types

Cell density of each cluster across all brain regions was defined as cell number in the region divided by the region area size. We plotted the cluster-density-by-region heatmap and found specific patterns for F1, V1 and temporal pole. Brain slides were then filtered for regions involved in the specific patterns to guarantee that these regions take an appropriate ratio in a slide. After that, we permutated the cluster labels 1000 times so that a background distribution of cluster-region pair could be obtained. The observed frequency of a specific cluster-region pair was compared with the background and the ratio of the observed value smaller than the background was calculated as the empirical p value. Finally, clusters were filtered with p = 0 and other quality criteria such as 1) no more than 20% regions showed significant co-occurrence with this cluster, 2) cluster cell number (at least 30 cells per slide) and 3) the observed ratio of the cluster in the specific region (larger than 0.3 for F1 and V1; larger than 0.5 for temporal pole).

Correlation of cell-type distribution with cortical hierarchy levels

The cortical regions in the visual system and somatosensory system were included to perform cell type proportion analysis. The hierarchy levels of visual or somatosensory cortices were derived from Felleman and Van Essen.[34] The cell proportion of individual cell type was calculated for each cortical region (cell counts of specific cell type / total cell counts of all cell types), and then the Spearman analysis was applied to calculate the correlation of cell type proportion with the hierarchy levels. The identified cell types whose proportion were positively or negatively correlated with the hierarchy levels in the visual and somatosensory systems (Spearman correlation, $R > 0.6$ or $R < -0.6$) were shown in heatmap (cell types were grouped into glutamatergic, GABAergic, or non-neuronal major class, and cortical areas were ordered by their hierarchy levels). To globally display the cell type distribution along the hierarchy, all the positively/negatively correlated cell types in each of the major class of cell types were accumulated and 3D surface rendered in the visual and somatosensory system and shown in Figure 3G. GO enrichment analysis was performed using marker genes of positively or negatively correlated cell types by metascape (https://metascape.org/) with the human dataset as reference.

Spatial distribution of neurotransmitter and neuromodulator receptor genes

We calculated the average expression values of these neurotransmitter receptors genes at six layers corresponding to 143 brain regions for all glutamatergic or GABAergic neurons based on the "sctransform" normalized spatial transcriptome matrix. We focused on the expression of these receptor genes in brain regions of the visual and somatosensory systems. For visualization of these gene expression in the GABAergic neurons, z-score normalization was performed for each gene among different cortical regions.

Calculation of glutamatergic neuron neighbor of CHC subpopulations in different cortical regions

All cell types in the 400 x 400 μm^2 square around each of the CHC cells in each cortical region were considered as their observation neighbors, and all cells in that cortical region were used as the background dataset and randomization test were performed for 500 times samplings. Each time, equivalent cell number to the total number of their observation neighbors were selected as their random neighbors; then, the rank sum test was performed to compare the observation neighbors with the random neighbors. When the appearing frequency of the observation neighbors around the CHC type was statistically higher than that of the random neighbors ($P < 0.05$), it was considered that the currently detected observation neighbors were the accompany neighbors for the CHC type in the observed brain region. The accompany glutamatergic neuron neighbor of CHC subpopulations was calculated in each cortical region.

Comparison of layer-specific astrocytes

From the spatial transcriptome data, we calculated the cell density in 6 layers of cell types from the whole brain areas. The cell density was the cell number to layer area size of each cell type. Then we obtained two layer1-specific ASC and one layer6-specific ASC, and identified the differential expressed genes with "sc.tl.rangk_genes_groups" function of scanpy from snRNA data. Genes were kept with the cutoff of log_2 fold-change > 1 and FDR < 0.01. In the two differential gene comparisons, the consensus up-regulated or down-regulated genes were further used to do functional enrichment analysis by metascape (https://metascape.org/) with the human dataset as reference.

Pseudotime trajectory analysis of oligodendrocyte lineage

We constructed the development trajectory using 2 types of Oligodendrocyte precursor cells (OPC) and 9 types of oligodendrocytes (OLG) from snRNA data with the R package monocle 2 (v.2.20.0). First, "negbinomial.size" function was performed for the raw mRNA counts matrix of OPC and OLG cells. Genes used for ordering the cells along the trajectory were kept with average expression > 0.1. The significant genes were calculated by the function "differentialGeneTest" function and selected with a qval cutoff of less than 0.01. We divided these genes into 4 groups, and performed functional enrichment analysis using R package clusterProfiler (v.4.0.5).

Reconstruction of the 3D cell atlas

A total of 119 coronal sections at different coronal coordinates from monkey #1 were used to recover the original shape and topology of a macaque brain. Firstly, we rotated all sections at bin 400 (0.2mm) manually. For the series of sections, a 2D rigid body transformation was computed between adjacent sections. The operation was iterated several times until all sections were aligned to the intermediate sections. Then the sections were assembled to create an initial 3D reconstructed data set, and then the stacked macaque brain volume was aligned to the existing D99 macaque atlas (https://afni.nimh.nih.gov/pub/dist/doc/htmldoc/nonhuman/macaque_tempatl/atlas_d99v2.html) by an affine transformation. Based on the initial 3D reconstruction, the corresponding sections and MRI images were aligned separately. Finally, all the transformation were applied to the coordinates of single cells at the spatial transcriptome map. A 3D spatial transcriptome atlas at the single-cell resolution of the entire macaque brain were thus created and used to visualize the spatial distribution of various cell types.

To illustrate cell profiling in different cortical regions, we used Workbench Command,[81] which is a set of command line tools used to perform various operations. First, the cell profiles were first normalized across cortical regions. Then the volumes of cell profiles which included 143 cortical regions based on D99 atlas macaque atlas (https://afni.nimh.nih.gov/pub/dist/doc/htmldoc/nonhuman/macaque_tempatl/atlas_d99v2.html) were converted to GIFTI file format in order to convert volumetric coordinates to surface coordinate system.the wb_command -volume-to-surface-mapping function and ribbon constrained mapping algorithm were used to execute this operation. Finally, the processed data was rendered to the surface of macaque brain carried by Matlab.

Cross-species analysis of different cell types

Public human PFC single nucleus data from human were download from GEO dataset.[48] Public human V1 single nucleus data were download from a previously published GEO dataset.[49] Public mouse PL-ILA-ORB (compared with PFC regions in human and macaque) and V1 10xv2 single cell data were download from https://portal.brain-map.org/atlases-and-data/rnaseq/mouse-whole-cortex-and-hippocampus-10x.[16] Human and mouse snRNA-seq data for F1 region was retrieved from a previously published cross-species comparison dataset.[12] Cells from PFC regions in human and macaque, and cells from PFC/F1/V1 regions in human, macaque and mouse were selected, then classified into glutamatergic neuron, GABAergic neuron, and non-neuronal cells. Only the glutamatergic neurons were used in further analysis. As the mouse only has a small amount of medial and orbital prefrontal cortex, and none of the vast lateral, dorsal or rostral prefrontal areas that exist in primates, so we also selected 32, 25 and 13 regions in the human and macaque cortex, which corresponded to PL, ILA and ORB regions in the mouse cortex, respectively, for a more stringent cross-species comparison. Public single nuclei transcriptome data of human 32, 25 and 13 regions were downloaded from https://www.biorxiv.org/content/10.1101/2022.10.12.511898v1.

Because of the coarse cell type annotation of human data, we further split the human cell type clusters in a iteration way, using a home-made modified IterCluster function from scrattch.hicat package, with parameters de_param (q1.th = 0.4, q.diff.th = 0.7, lfc.th = 0.5, de.score.th = 150, min.cells = 20, min.genes = 4). Integration of three species excitatory neurons were done by Seurat IntegrateData with marker genes as anchorset. which were found by select_markers function of scrattch.hicat package. The

integrated cells were further clustered using Seurat FindClusters with resolution = 3. Cell subclasses were manually annotated based on the marker genes. Marker genes for subclasses of each species were calculated using Seurat FindAllMarkers with default parameters. Cell types overlapping ratio of different species were calculated following the scripts of the publish pipeline.[12] Differential gene expression calculation of 6 primate-specific cell types between other macaque cells were done by Seurat FindAllMarkers function. A total of 226 genes with adjust (wilcox-test, bonferroni correction) *P value* < 0.05 and log$_2$ fold change > 0.5 in any one of six primate-specific cell types were selected as highly expressed genes for subsequent functional enrichment analysis using clusterProfiler enrichGO function based on human database org.Hs.eg.db.

QUANTIFICATION AND STATISTICAL ANALYSIS

No statistical methods were used to predetermine sample sizes, but the sample sizes here are similar to those reported in previous publications. No randomization was used during data collection as there was a single experimental condition for all acquired data. Data collection and analyses were not performed blind to the conditions of the experiments as all experiments followed the same experimental condition. Statistical details of experiments and analyses can be found in the figure legends and main text above. All statistical tests were two-sided, and statistical significance was considered when *P value* < 0.05. To account for multiple-testing, the *P value*s were adjusted using the bonferroni correction.

Supplemental figures
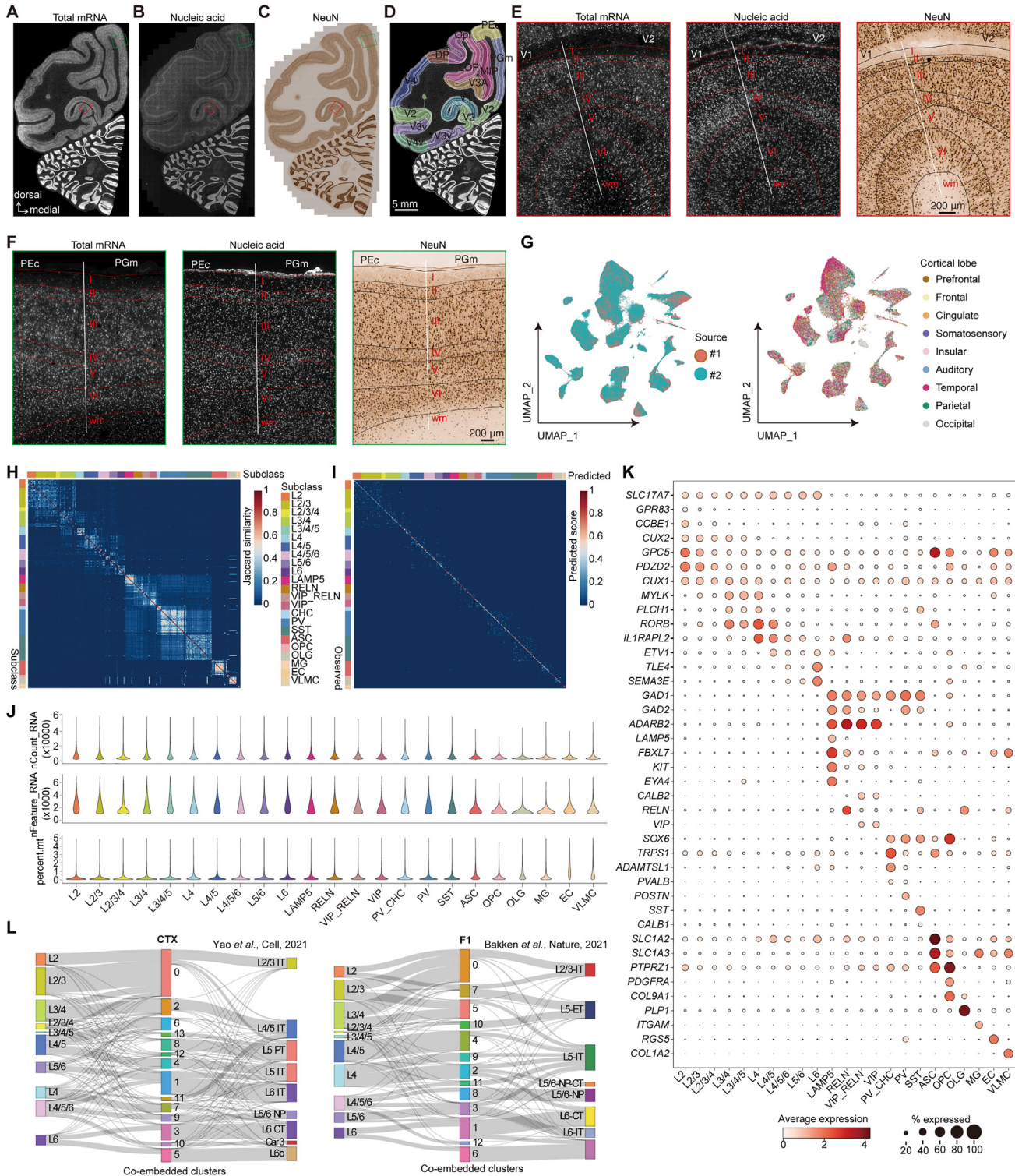
(legend on next page)

Figure S1. Regional parcellation and cell-type identification, related to Figure 1

(A and B) (A) Total mRNA captured and (B) staining for nucleic acid from an example section.

(C) NeuN staining of an adjacent section to (A).

(D) Region- and layer-parcellation contours.

(E and F) Parcellation of cortical layers and V1 and V2 (E) and PEc and PGm (F) regions based on cytoarchitectual pattern, enlarged from the red and blue boxed areas in (C), respectively.

(G) UMAP layout showing single cells from different monkeys (left) and cortical lobes (right).

(H) Heatmap showing Jaccard similarity of marker genes among various cell types.

(I) Heatmap showing the prediction scores of various cell types using random forest.

(J) Violin plot showing the single-cell quality of subclasses.

(K) Dot plot showing marker gene expression for all the subclasses in Figure 1B.

(L) Sankey plot depicting correspondence between our glutamatergic subclasses and published projection-property-inferred glutamatergic subclasses.[12,16]
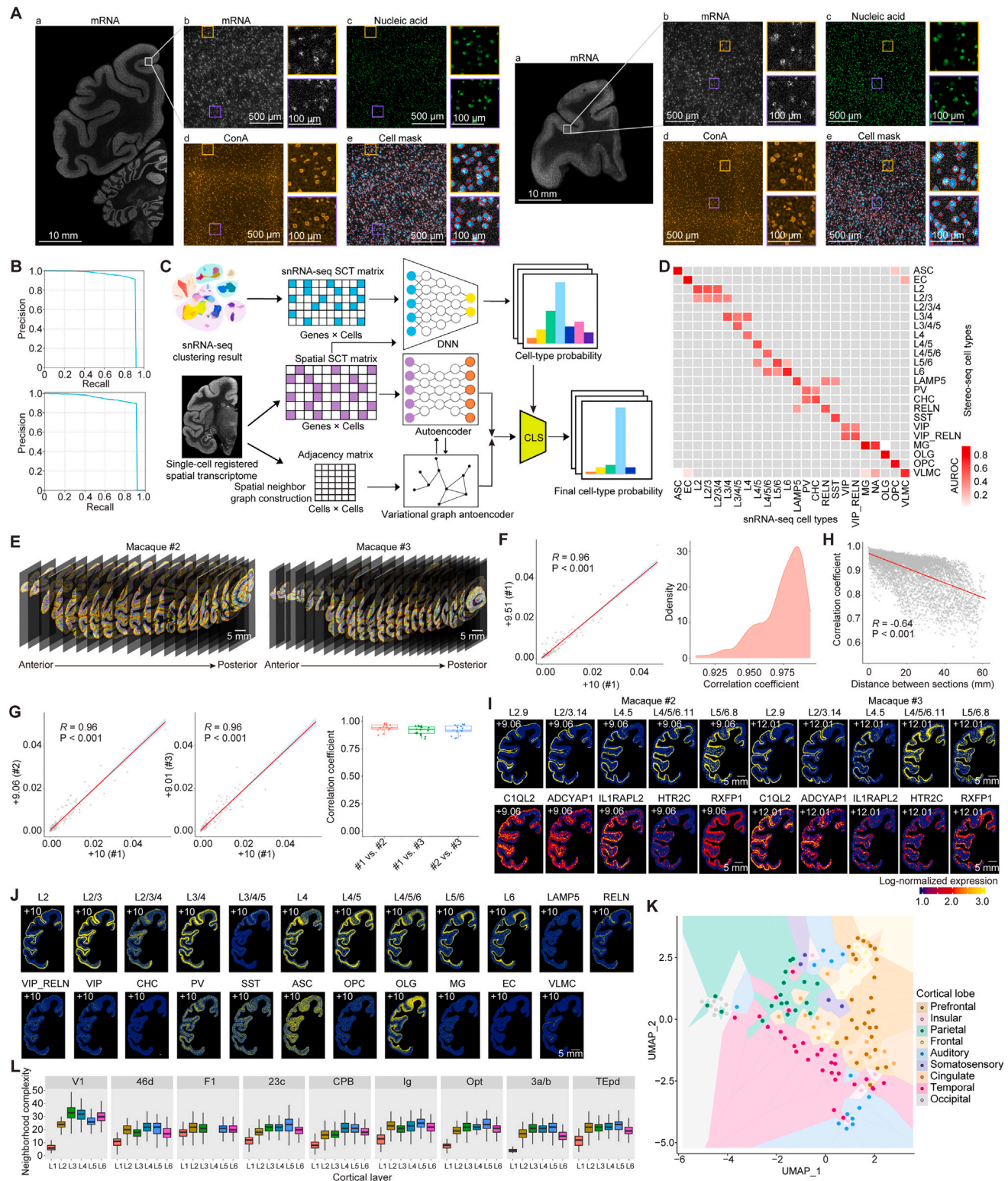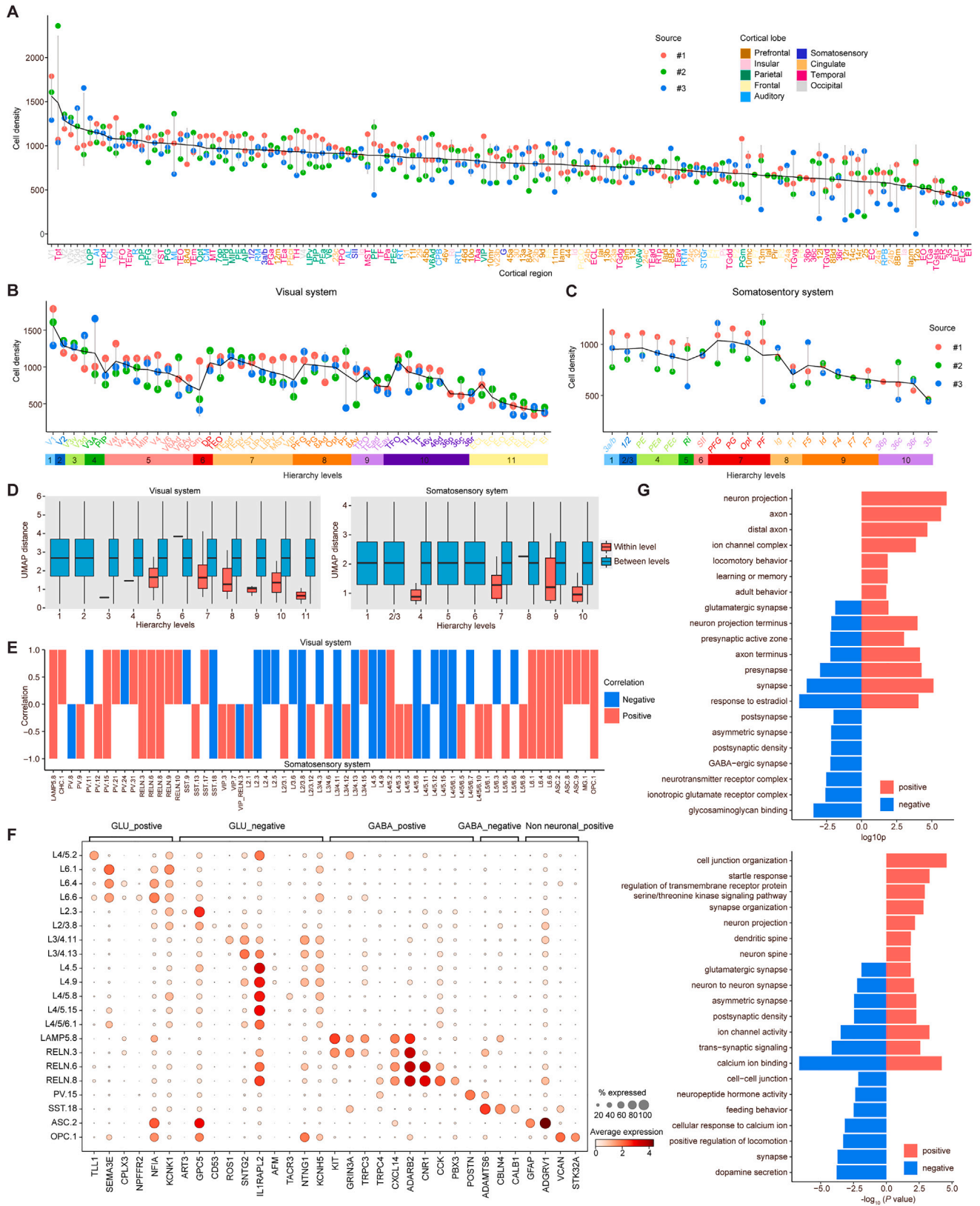
Figure S2. Stereo-seq single-cell registration and cell-type annotation, related to Figure 2

(A) Illustration of single-cell segmentation in stereo-seq data. (Aa) Total RNA captured from sections with EBZ coordinate at 0 (left) and +33.08 (right). Images show total mRNA (Ab), staining for nucleic acid (Ac) and ConA (Ad), and cells identified (Ae). Enlarged orange and purple boxes show finer resolution images. (B) Recall and precision curve of cell segmentation for the regions in (Ab).

(legend continued on next page)

(C) Illustration of deep-learning-based cell-type-registration process.

(D) Correspondence between subclasses determined by snRNA-seq and stereo-seq.

(E) Spatial map of 264 cell types in all sections from macaque #2 (left) and #3 (right).

(F) Correlation of cell-type distributions between two adjacent sections at EBZ +10 (left) or any two adjacent sections (right) from monkey #1.

(G) Correlation of cell-type distributions in sections at similar coordinates from different monkeys.

(H) Relationship between correlation coefficients of cell-type distributions and distances between sections.

(I) Spatial map of five cell types and marker genes in a representative section of macaque #2 and #3.

(J) Spatial map of 23 cell subclasses in a representative section.

(K) UMAP of regional cell-type compositions using snRNA-seq data.

(L) Comparison of composition complexity among cortical layers in 9 brain regions.

A

B — Visual system
C — Somatosentory system

D

E — Visual system / Somatosensory system

F
GLU_positive   GLU_negative   GABA_positive   GABA_negative   Non neuronal_positive

G

(legend on next page)

Figure S3. Cell-type distribution across hierarchies, related to Figure 3

(A) Cell density in 143 brain regions.

(B and C) Cell density in brain regions ordered by hierarchical levels in visual (B) and somatosensory (C) systems.

(D) Boxplot showing relative distances between regions in the UMAP of Figure 3C and 3D.

(E and F) (E) Bar plot showing cell types with positive or negative correlations with hierarchical levels and (F) dot plot showing marker gene expression of the cell types in (E).
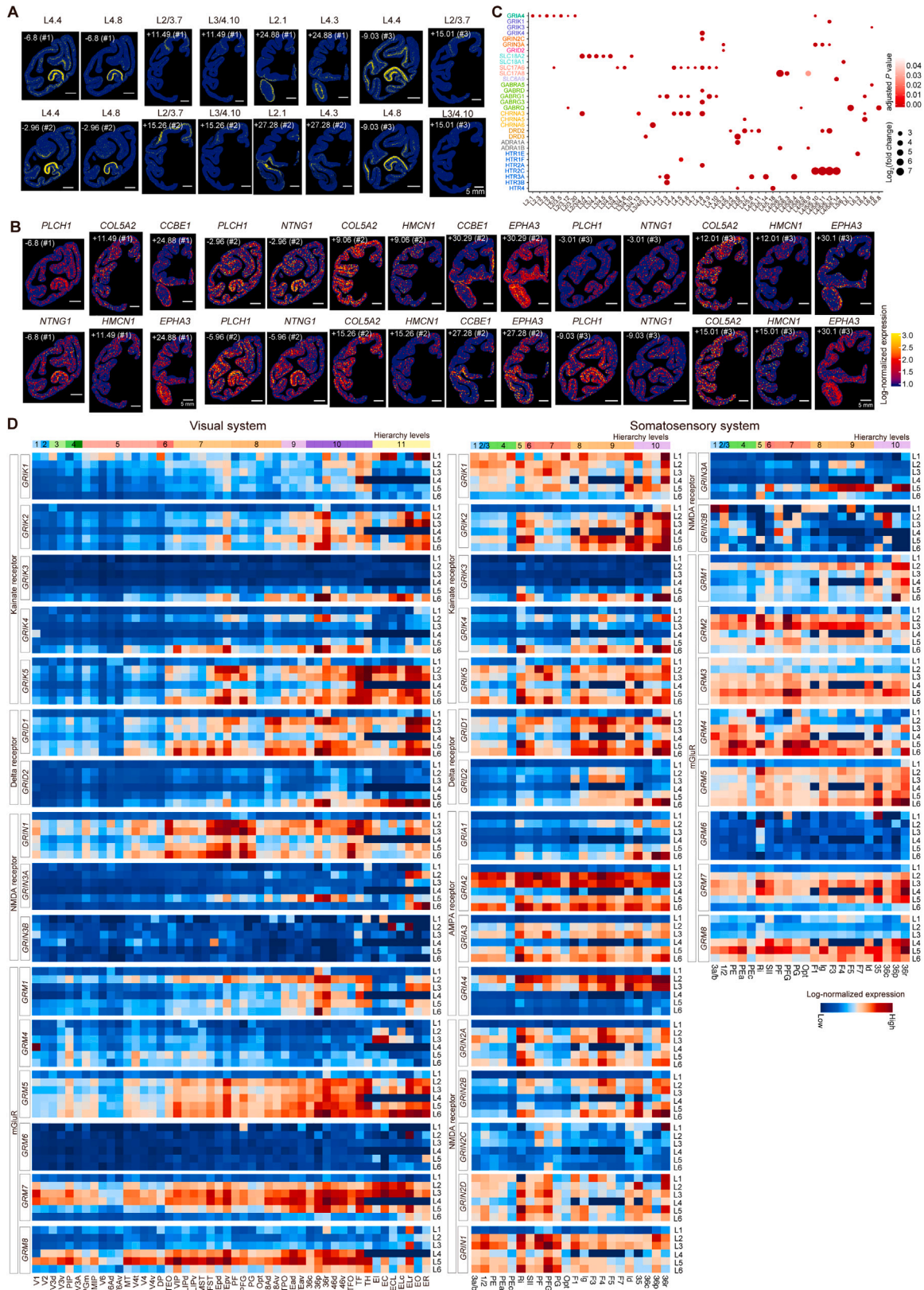
(G) GO terms for the genes in (F).

Figure S4. Distribution of glutamatergic cell types, related to Figure 4

(A) Six example glutamatergic cell types in V1, F1, and temporal pole.

(B) Marker gene patterns for the region-specific cell types in (A).

(C) Dot plot showing glutamatergic receptor gene expression in glutamatergic cell types.

(D) Gene expression levels of AMPA, NMDA, Kainate, Delta, and metabotropic glutamate receptor subunits in different layers along hierarchies. Expression level was normalized for each gene and color coded in log scale.
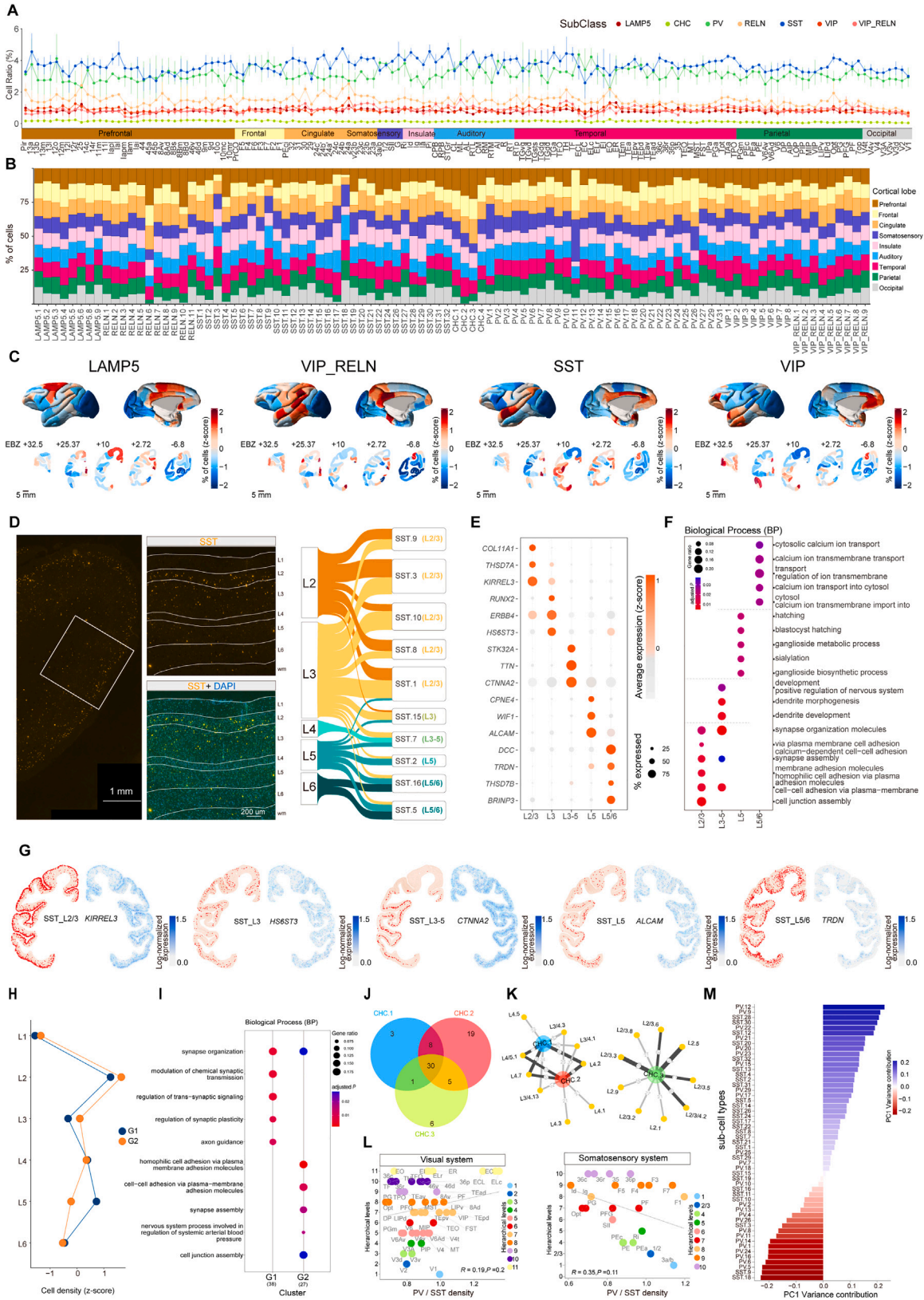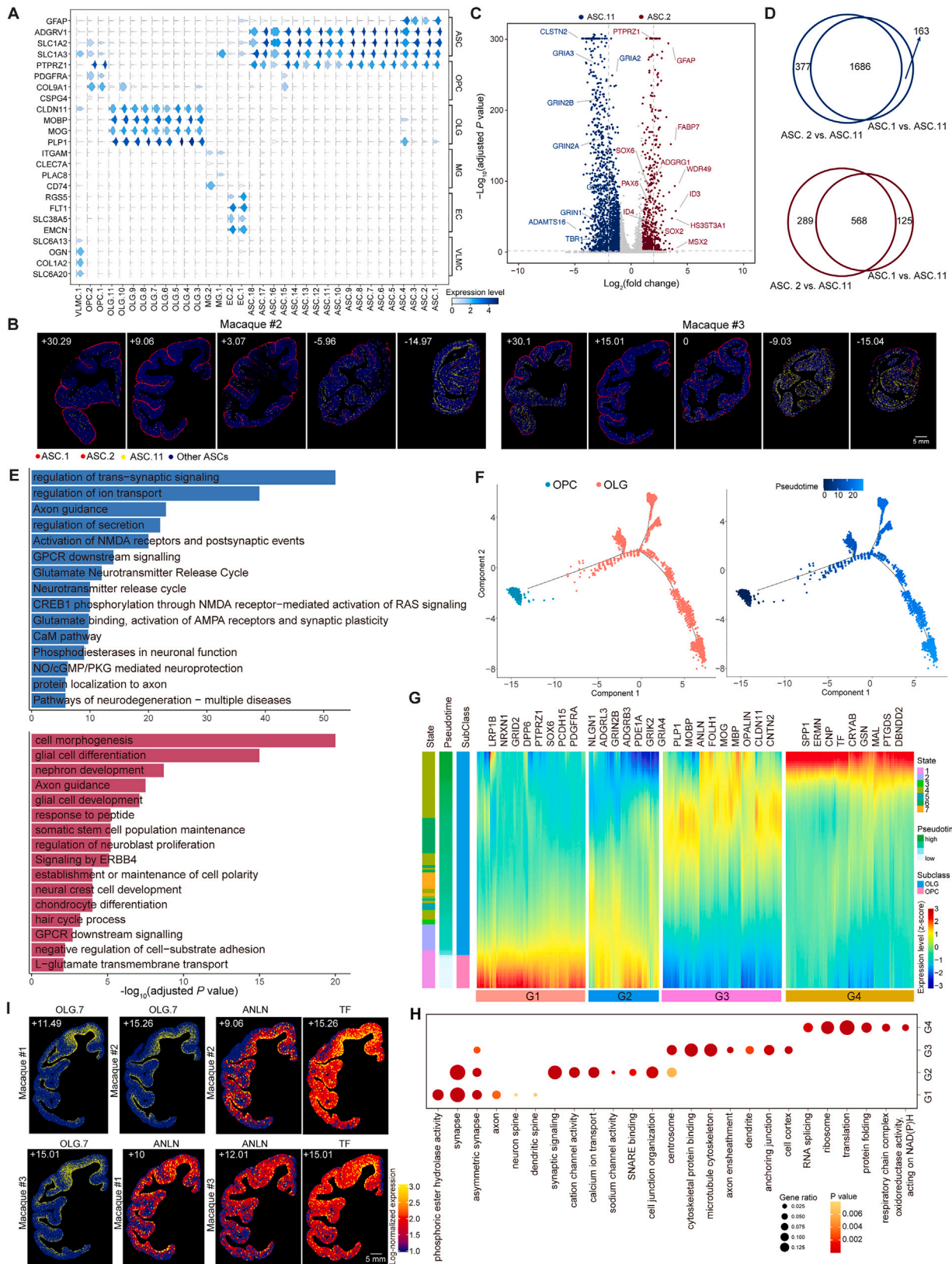
(legend on next page)

Cell
Resource

Figure S5. GABAergic cell types, related to Figure 5

(A) Relative regional distribution of GABAergic subclasses.

(B) Stack-bar plots showing the percentage of each GABAergic cell type among 9 cortical lobes.

(C) 3D (upper) and 2D (bottom) distributions of GABAergic cell subclasses.

(D) SST cell distribution. Left, RNAscope and DAPI staining for *SST*. Right, Sankey plot of SST cell laminar distribution.

(E) Dot plot showing the laminar expression patterns of marker genes for SST cell types.

(F) GO terms for the genes in (E).

(G) Laminal distribution of SST cell types (left) and marker gene expression (right).

(H) Relative abundances of two SST cell groups in each cortical layer.

(I) GO terms among DEGs in G1- and G2-SST cells.

(J) Venn diagrams showing the number of neighborhood glutamatergic cell types shared across CHC cell types.

(K) Top neighborhood glutamatergic cell types of three CHC cell types.

(L) Correlation between the relative densities of PV and SST cell types.

(M) Weight of various PV and SST cell types to PC1 shown in Figure 5J.

(legend on next page)

Figure S6. Non-neuronal cell types, related to Figure 6

(A) Violin plot showing marker gene expression for non-neuronal cell types.

(B) Spatial distribution of ASCs in 5 sections of macaque #2 and #3.

(C) Volcano plot showing DEGs in ASC.2 and ASC.11.

(D) Venn diagrams showing DEGs overlap between ASC.11 and ASC.1 or ASC.2.

(E) GO terms enriched among DEGs between L1- and L6-enriched ASCs.

(F) UMAP showing oligodendrocyte differentiation and maturation trajectory.

(G) Heatmap showing marker gene expression along oligodendrocyte trajectory.

(H) Dot plot showing GO terms associated with the 4 groups of genes in (G).

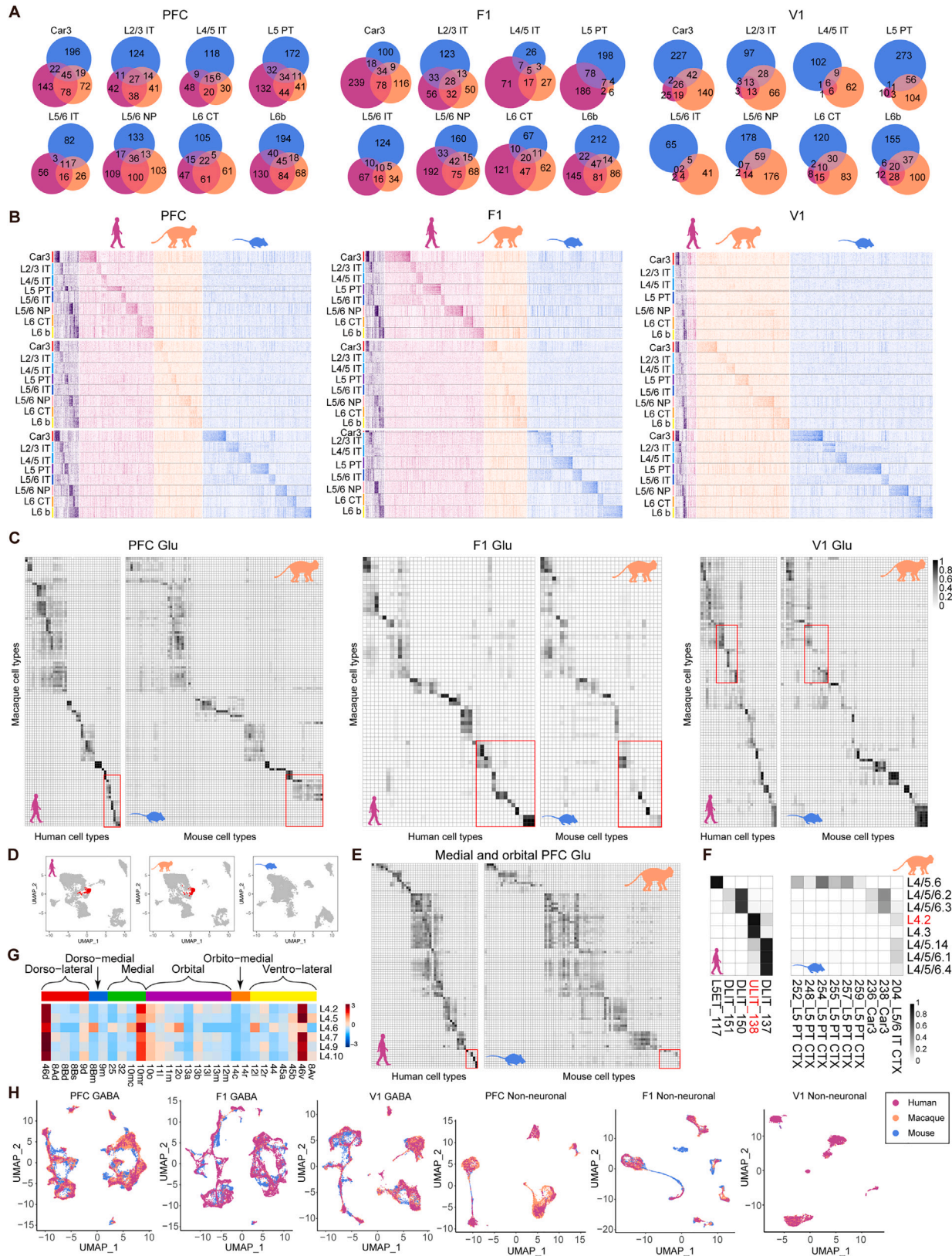(I) Spatial map showing a F1-enriched OLG cell type and two marker genes.

Figure S7. Cross-species comparison of glutamatergic neurons, related to Figure 7

(A and B) Venn diagrams (A) and heatmaps (B) showing convergent/divergent marker genes and their expression levels for 8 major cell subclasses in PFC, F1, and V1 of three species.

(C) Pairwise comparison of glutamatergic cell types. Red-marked parts were enlarged in Figures 7A–7C.

(D) UMAP of integrated snRNA-seq/scRNA-seq data for glutamatergic neurons from regions 32, 25, and 13 of macaque and humans and PL-ILA-ORB regions of mice. Red-labeled types are absent in mice.

(E and F) Pairwise comparison of glutamatergic cell types (Table S7) (E), and zoom-in view of the red box in (F), with primate-specific types labeled in red.

(G) Regional distribution of primate-specific cell types in macaque PFC.

(H) UMAP of integrated snRNA-seq/scRNA-seq data of GABAergic and non-neuronal cells for PFC, F1, and V1 across species.